

1
2
3
4
5
6
7
8
9
10
11
12
13
14
15
16
17
18
19
20

Revision 1

Parameterized lattice strain models for REE partitioning between amphibole and silicate melt

Kei Shimizu^{1*}, Yan Liang¹, Chenguang Sun², Colin R. M. Jackson³, and Alberto E. Saal¹

¹Department of Earth, Environmental and Planetary Sciences, Brown University,
Providence, RI 02912, USA

²Department of Earth Science, Rice University, TX 77005, USA

³Smithsonian Institution, DC 20013, USA

*Corresponding author. Current address: Department of Terrestrial Magnetism, Carnegie
Institution of Washington, 5241 Broad Branch Road, NW, Washington, DC 20015, USA
Email address: kshimizu@carnegiescience.edu (K. Shimizu)

21

Abstract

22 The distribution of rare earth elements (REEs) between amphibole and silicate melt is
23 important for understanding a wide variety of igneous and metamorphic processes in the
24 lithosphere. In this study, we used published experimental REE and Y partitioning data
25 between amphibole and silicate melt, the lattice strain model, and non-linear least squares
26 regression method to parameterize key partitioning parameters in the lattice strain model
27 (D_0 , r_0 , and E) as a function of pressure, temperature, and both amphibole and melt
28 compositions. Two models, which give nearly identical results, are obtained in this study.
29 In the first model, D_0 depends on temperature and amphibole composition: it positively
30 correlates with Ti content, and negative correlates with temperature and Mg, Na, and K
31 contents in the amphibole. In the second model, D_0 depends solely on the melt
32 composition: it positively correlates with Si content, and negatively correlates with Ti
33 and Ca contents in the melt. In both the mineral and melt composition models, r_0
34 negatively correlates with the ferromagnesian content in the M4 site of the amphibole and
35 E is a constant. The very similar coefficients in the equations for r_0 and best-fit values for
36 E in the two models allow us to connect the two models through amphibole-melt phase
37 equilibria. An application of our model to amphiboles in mantle xenoliths shows that
38 observed major element compositional variations in amphibole alone can give rise to
39 order of magnitude variations in amphibole-melt REE partition coefficients. Together
40 with experimental data simulating fractional crystallization of arc magmas, our models
41 suggest that (1) REE partition coefficients between amphibole and melt can vary by an
42 order of magnitude during arc magma crystallization due to variation in the temperature
43 and composition of the amphibole and melt, and that (2) amphibole fractional

44 crystallization plays a key role in depleting the middle REEs relative to heavy REEs and
45 light REEs in arc magmas.

46

47

Keywords

48 REE and Y partition coefficients; amphibole; amphibole melting in the mantle;
49 amphibole fractional crystallization

50

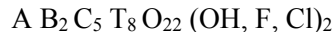
51

1. Introduction

52 Amphibole is ubiquitous in the Earth's lithosphere, occurring in a wide variety of
53 igneous and metamorphic rocks. As an inosilicate, amphibole has three main structural
54 sites (A, M4, and M1-M3) that can accommodate cations of a range of size and charge.

55 The general chemical formula of amphiboles may be described by the expression

56



57 where A = Na, K, or vacant (\square) in A site; B = Ca, Na, Mn, Fe²⁺, Mg in M4 site; C =

58 Fe²⁺, Fe³⁺, Mg, Al, Mn, Ti, Cr, in M1, M2, and M3 sites; T = Si, Al in tetrahedral site

59 (Hawthorne, 1983). The smaller M1-M3 sites are in 6-fold coordination, while the larger

60 M4 site is in 8-fold coordination. The latter can accommodate larger cations such as the

61 trivalent rare earth elements (REE) and Y (ionic radii 0.977–1.16 Å, 8-fold coordination,

62 Shannon (1976)), while the smaller M1-M3 sites can accommodate smaller cations such

63 as high-field strength elements.

64 The subject of the present study is REE partitioning between amphibole and
65 silicate melt, which is important to understand the generation and differentiation of
66 hydrous magmas. According to the lattice strain model (Blundy and Wood, 1994; Brice,

67 1975; Wood and Blundy, 1997), the partition coefficients of trivalent REEs between
68 amphibole and silicate melt vary systematically with their ionic radii:

$$69 \quad D_j^{\text{amph-melt}} = D_0 \exp \left[-\frac{4\rho EN_A}{RT} \left(\frac{r_0}{2} (r_0 - r_j)^2 - \frac{1}{3} (r_0 - r_j)^3 \right) \right], \quad (1)$$

70 where D_0 is the amphibole-melt partition coefficient for the strain-free substitution; r_0 is
71 the radius of a hypothetical cation that substitutes into the site with zero strain; r_j is the
72 ionic radius of the element of interest; E is the effective Young's modulus for the lattice
73 site; N_A is Avogadro's number; R ($= 8.3145 \text{ J mol}^{-1} \text{ K}^{-1}$) is the gas constant; and T is
74 temperature in Kelvin. The lattice strain parameters (D_0 , r_0 , E) are, in general, a function
75 of pressure (P), temperature (T), and composition (X).

76 Amphibole-melt REE partition coefficients have been shown to negatively
77 correlate with T (Green and Pearson, 1985; Klein et al., 1997; Nandedkar et al., 2016;
78 Nicholls and Harris, 1980) and P (Adam and Green, 1994; Adam and Green, 2003; Dalpé
79 and Baker, 2000; Green and Pearson, 1985), and positively correlate with the degree of
80 melt polymerization (Brophy, 2008; Green and Pearson, 1985; Klein et al., 1997;
81 Nandedkar et al., 2016; Nicholls and Harris, 1980; Tiepolo et al., 2007; Tiepolo et al.,
82 2000). The effect of amphibole crystal chemistry on amphibole-melt REE partition
83 coefficients has also been observed in previous studies. For example, greater occupancy
84 of the A site by Na and K were shown to decrease the partition coefficients, presumably
85 suggesting substitution of REEs in place of Na and Ca in the M4 site charge compensated
86 by a vacancy in the A site (e.g., $\text{Ca}_{\text{M4}}^{2+} \text{K}_{\text{A}}^{+1} \leftrightarrow \text{REE}_{\text{M4}}^{3+} \square_{\text{A}}$) (Brenan et al., 1995; Green and
87 Pearson, 1985; Nicholls and Harris, 1980). Also, amphibole-melt REE partition
88 coefficients have been demonstrated to correlate with the amphibole-melt partition

89 coefficient of Ca (Hilyard et al., 2000; Klein et al., 1997; Sisson, 1994). These
90 correlations have been used to build empirical models of amphibole-melt REE partition
91 coefficients (Sisson, 1994; Tiepolo et al., 2007; Tiepolo et al., 2000). These previous
92 models are useful for predicting the REE and Y partition coefficients when the
93 equilibrium melt composition (Sisson, 1994; Tiepolo et al., 2007; Tiepolo et al., 2000) or
94 amphibole-melt major element partition coefficients (Hilyard et al., 2000) are available.
95 These models are difficult to implement, however, for natural amphiboles such as those
96 found in cumulates and xenoliths where melt composition is not available. Further,
97 previous models parameterized partition coefficients for individual elements
98 independently, so each element requires a different set of model coefficients. This makes
99 it difficult to understand the general behavior of REE partitioning in amphibole and to
100 develop accurate models for elements with sparse partitioning data (such as Gd and Tm).
101 In addition these empirical models require a large number of coefficients to describe the
102 partitioning of all the REEs and Y.

103 In this study, we present the first parameterized lattice strain models for REE and
104 Y partitioning between amphibole and silicate melt for a range of P , T , melt and
105 amphibole compositions. These models are developed following a new protocol that has
106 been successfully used to develop parameterized lattice strain models for REE and Y
107 partitioning between major rock-forming minerals (clinopyroxene, orthopyroxene, garnet,
108 olivine, and plagioclase) and basaltic melts (Dyger et al., 2014; Sun et al., 2017; Sun and
109 Liang, 2012; Sun and Liang, 2013a; Sun and Liang, 2013b; Yao et al., 2012). We
110 develop two parameterized lattice strain models, one of which is described by T and
111 mineral composition, and the other is fully captured by melt composition. We reconcile

112 the two models through amphibole-melt equilibria, and, as a byproduct, develop a new
113 thermometer for calculating the amphibole liquidus. As geochemical applications of our
114 models, we (1) evaluate the ranges of amphibole-melt REE partition coefficients in
115 mantle amphiboles using observed amphibole compositions in mantle xenoliths, and (2)
116 calculate the REE concentration in experimental melts that simulate fractional
117 crystallization of arc magmas to evaluate the effect of amphibole fractional crystallization
118 on the REE concentration in arc magmas.

119

120

2. Method

2.1. Data compilation

122 REE and Y partitioning data for amphibole and silicate melts were compiled from
123 published experimental studies. The data were filtered on the basis of attainment of
124 equilibrium (e.g., absence of core to rim variation, sector zoning in major elements,
125 absence of melt inclusions in the analyzed volume, and run duration), misfits or outliers
126 with reference to the lattice strain model (e.g., Eu anomaly), following the procedure
127 established in the previous studies (Dygart et al., 2014; Sun and Liang, 2012; Sun and
128 Liang, 2013b; Yao et al., 2012). Experimental data that were analyzed using an ion probe
129 and laser ablation inductively coupled mass spectrometry (LA-ICP-MS) were inspected
130 for their quality by plotting the partition coefficients of similarly incompatible element
131 pairs (e.g., La-Ce, Eu-Nd, and Lu-Yb, example shown in supplementary Fig. S1). In
132 these plots, most partitioning data follow a well-defined correlation suggesting high
133 quality and internally consistent analysis while some partitioning data significantly
134 deviate off the trend. The off-trend partitioning data were excluded as they suggest either

135 presence of Eu anomalies, poorly equilibrated experiments, or low quality analysis. This
136 method could not be used to inspect the quality of highly doped experiments analyzed
137 using an electron microprobe (EMP) as they often contain fewer than 3 elements that are
138 far from each other in incompatibility. Furthermore, the studies of Adam and Green
139 (1994) and Klein et al. (1997) showed evidence of Henry's law behavior of REEs in their
140 doped experiments by running an undoped experiment at the same *P-T-X* conditions,
141 while the study of Hilyard et al. (2000) did not show any evidence for this. As shown
142 later in this study, however, the partitioning data of Hilyard et al. (2000) follow our
143 partitioning models in the same manner as other partitioning data, suggesting the Henry's
144 law behavior of REEs in their experiments. Hence, we included the partitioning data from
145 Hilyard et al. (2000) in our dataset.

146 Following the data selection procedure outlined above, we obtained 556
147 partitioning data from 100 experiments reported in 9 studies (Adam and Green, 1994;
148 Adam and Green, 2003; Adam and Green, 2006; Dalpé and Baker, 2000; Hilyard et al.,
149 2000; Klein et al., 1997; LaTourrette et al., 1995; Nandedkar et al., 2016; Tiepolo et al.,
150 2000). Table 1 summarizes the selected partitioning studies that were used to calibrate the
151 model described below. The selected 100 experiments were conducted at 780–1100°C
152 and 0.2–2.5 GPa. These experiments produced calcic amphiboles and melts with large
153 variations in composition (e.g., Si = 5.74–7.27 a.p.f.u. in amphibole, Mg# = 36.5–100 in
154 amphibole, Mg# = 1.9–100 in melt, SiO₂ = 34.14–68.7 wt% in melt; see Fig. 1 and Table
155 1 for details) and partition coefficients (e.g., $D_{La} = 0.03–0.59$, $D_{Sm} = 0.27–5.56$, $D_{Lu} =$
156 $0.28–6.77$) (Fig. 2). The compositional variations in the experimental amphiboles and

157 melts cover a large portion of those in natural samples from arc and intraplate settings
158 and mantle xenoliths (Figs. 1a–f).

159

160 **2.2. Parameterization method**

161 To develop a parameterized model for trivalent REE and Y partitioning between
162 amphibole and silicate melt, we conducted a multivariable nonlinear least squares
163 analysis. Following the procedure of recent studies on mineral-melt REE partitioning
164 (Dygart et al., 2014; Sun and Liang, 2012; Sun and Liang, 2013a; Yao et al., 2012), we
165 conduct the least squares analysis in two steps: (1) identification of key variables that
166 affect D_0 , r_0 , and E in the lattice strain model through least squares analysis of individual
167 experiments, and (2) simultaneous inversion of all the filtered experimental data using the
168 primary variables identified in step (1). An important advantage of step (2) is that it
169 allows us to include experiments that reported only one or two trace elements and hence
170 they can be used to calibrate the three-parameter lattice strain model in step (1) (see
171 supplementary Fig. S2 and S3 for experiments from Hilyard et al. (2000) and Klein et al.
172 (1997)). We assume that REEs and Y enter the M4 site in amphibole, and use eightfold
173 coordinated ionic radii from Shannon (1976). We did not distinguish between the M4 and
174 M4' sites (Bottazzi et al., 1999) given the lack of evidence of the two-site occupancy of
175 the REEs in amphibole in our data. We assumed that D_0 in the lattice strain model has the
176 simple form

$$177 \quad \ln D_0 = a_0 + \frac{a_1}{RT} + f\left(X, \frac{P}{T}\right), \quad (2)$$

178 where a_0 and a_1 are constants to be determined, and f is a function of mineral and melt
179 composition and P/T . The r_0 is assumed to be a function of mineral composition as it

180 correlates well with the amphibole composition. We explored the composition and r_0
181 dependence of E observed for other minerals (Sun and Liang, 2012; Sun and Liang,
182 2013b; Yao et al., 2012), but it shows only small variation for amphibole and does not
183 correlate well with amphibole composition or r_0 . Hence, E was assumed to be a constant.

184 Through an extensive search of various permutations of the composition
185 variables, we found that D_0 can be described as a function of melt Si, Ti and Ca contents
186 or as a function of T and Ti, Mg, Na and K contents in amphibole. For convenience of
187 description, we refer to the latter as the mineral composition model and the former as the
188 melt composition model. In both models, ferromagnesian (sum of Mg, Fe^{2+} , and Mn^{2+} ,
189 designated as Fm hereafter) content in the M4 site of the amphibole is the main factor
190 affecting r_0 , while E is a constant. For the melt composition model, the lattice strain
191 parameters D_0 , r_0 , and E take on the following expressions:

$$192 \quad \ln D_0^{\text{amph}} = a_0 + a_1 \ln(X_{\text{Si}}^{\text{melt}}) + a_2 \ln(X_{\text{Ti}}^{\text{melt}}) + a_3 \ln(X_{\text{Ca}}^{\text{melt}}), \quad (3)$$

$$193 \quad r_0^{\text{amph}} = a_4 + a_5 X_{\text{Fm}}^{\text{amph-M4}}, \quad (4)$$

$$194 \quad E^{\text{amph}} = a_6. \quad (5)$$

195 For the mineral composition model, we have

$$196 \quad \ln D_0^{\text{amph}} = b_0 + \frac{b_1}{RT} + b_2 X_{\text{Ti}}^{\text{amph}} + b_3 X_{\text{Mg}}^{\text{amph}} + b_4 X_{\text{Na}}^{\text{amph}} + b_5 X_{\text{K}}^{\text{amph}}, \quad (6)$$

$$197 \quad r_0^{\text{amph}} = b_6 + b_7 X_{\text{Fm}}^{\text{amph-M4}}, \quad (7)$$

$$198 \quad E^{\text{amph}} = b_8, \quad (8)$$

199 where a_0, a_1, \dots, a_6 and b_0, b_1, \dots, b_8 in Eqs. (3)–(8) are constants determined by stepwise
200 multiple linear regression analyses of the lattice strain parameters (D_0 , r_0 , and E); $X_{\text{Ti}}^{\text{amph}}$,

201 $X_{\text{Mg}}^{\text{amph}}$, $X_{\text{Na}}^{\text{amph}}$, and $X_{\text{K}}^{\text{amph}}$ are cation numbers (per 23 oxygen) and $X_{\text{Fm}}^{\text{amph-M4}}$ is the Fe^{2+}
202 + Mn^{2+} + Mg content in the M4 site assuming all iron is present as ferrous iron; and $X_{\text{Si}}^{\text{melt}}$
203 , $X_{\text{Ti}}^{\text{melt}}$, and $X_{\text{Ca}}^{\text{melt}}$ are mole fractions of cations in the melt calculated on an anhydrous
204 basis assuming all iron is present as ferrous iron. The experiments used to parameterize
205 our model were performed at oxygen fugacities between QFM-2 to QFM+3.2 (where
206 QFM is the quartz-fayalite-magnetite buffer), which covers a large range of those found
207 in natural magmatic systems (Ballhaus, 1993; Kelley and Cottrell, 2009; Parkinson and
208 Arculus, 1999). Hence, our assumption of all iron in amphibole and melt being present as
209 ferrous iron is incorrect. Nevertheless, this simplification allows us to develop
210 parameterized lattice strain models for amphibole-melt REE partitioning without making
211 complicated assumptions with regard to the ferric iron content in the amphibole and melt.
212 Also, Na occupies both the M4 and A sites in amphibole, but we use the total Na content
213 for the mineral composition model. We attempted to use Na in the M4 and A sites as
214 separate variables, but the coefficients for the two variables are nearly identical, leading
215 us to use total Na content instead. Finally, we used the anhydrous basis for the melt as
216 another simplification because in some studies, H_2O contents in the melt are calculated
217 according to mass balance, which may introduce large uncertainties. These more
218 complicated but realistic treatment of amphibole and melt compositions should be
219 considered in future studies when knowledge of redox state, site occupancy and water
220 content becomes available.

221 To further improve the fit to the measured partitioning data and better assess the
222 uncertainties for the fitting coefficients, we performed global least squares analyses for
223 the melt composition and mineral composition models by substituting equations (3)–(5)

224 and (6)–(8) into Eq. (1), respectively. For the melt composition model (Eqs. (1), (3)–(5)),
225 we inverted the 6 coefficients (a_0, a_1, \dots, a_6) simultaneously through a global inversion of
226 the 556 filtered partitioning data. For the mineral composition model (Eqs. (1), (6)–(8)),
227 we inverted the 8 coefficients (b_0, b_1, \dots, b_8) simultaneously through a global inversion of
228 the same data used for the melt composition model. To carry out the global inversions,
229 we used the coefficients from the stepwise multiple linear regression as initial values in
230 the nonlinear least squares analysis and minimize the Chi-square as defined below:

$$231 \quad C_p^2 = \sum_{j=1}^N (\ln D_j - \ln D_j^m)^2, \quad (9)$$

232 where D_j is defined by Eq. (1) for element j , D_j^m is the measured amphibole-melt
233 partition coefficient for element j , and N (= 556) is the total number of measured
234 partitioning data used in this study. Since it is difficult to assess inter-laboratory
235 uncertainties arising from different experimental procedures and analytical methods in
236 the selected partitioning studies (Table 1), we did not weight the Chi-square using
237 reported uncertainties of measured partition coefficients. The latter are based solely on
238 chemical analysis of REE and Y in individual charges. Uncertainties due to temperature
239 gradient, oxidation state, water content and water loss, experimental reproducibility,
240 among others, maybe larger than the reported uncertainty. Hence Eq. (9) assumes equal
241 uncertainty for all the experimental data included in this study. This is an obvious
242 simplification, but can be judged by the quality of our best fit models for individual
243 samples (see supplementary Figs. S2 and S3).

244 Although convenient in nonlinear regression analysis, the absolute values of the
245 Chi-square defined by Eq. (9) depend on the number of data used in the inversion. To

246 assess the goodness of fit in a simple way, we calculated the Pearson's Chi-square (C_p^2)
247 after the inversion using the expression

$$248 \quad C_p^2 = \frac{\sum_{j=1}^N (D_j - D_j^m)^2}{D_j}. \quad (10)$$

249 A better predictive model should provide partition coefficients closer to measured values
250 and hence has a smaller C_p^2 . The results are shown in Fig. 3 and discussed below.

251

252

3. Results

253 The global fit to the 556 partitioning data from the 100 experiments produces two sets of
254 expressions for the lattice strain parameters for REE and Y partitioning in amphibole. For
255 the melt composition model, we have:

$$256 \quad \ln D_0^{\text{amph}} = -3.08(\pm 0.52) + 0.74(\pm 0.34) \ln(X_{\text{Si}}^{\text{melt}}) - 0.33(\pm 0.05) \ln(X_{\text{Ti}}^{\text{melt}}) \\ - 0.84(\pm 0.07) \ln(X_{\text{Ca}}^{\text{melt}}), \quad (11)$$

$$257 \quad r_0^{\text{amph}} = 1.045(\pm 0.003) - 0.048(\pm 0.009) X_{\text{Fm}}^{\text{amph-M4}}, \quad (12)$$

$$258 \quad E^{\text{amph}} = 341(\pm 18), \quad (13)$$

259 where r_0 is in Å; and E is in GPa; and numbers in parentheses are 2σ uncertainties
260 estimated directly from the simultaneous inversion. As D_0 defines the peak value of the
261 parabola in the lattice strain model (Eq. (1)), the melt composition model indicates REE
262 partition coefficients in amphibole increase with the increase of Si content in the melt and
263 decrease with the increase of Ti and Ca content in the melt. Figs. 4a–c show that the
264 amphibole-melt Sm partition coefficient positively correlates with Si and negatively
265 correlates with Ti and Ca contents in the melt. The Si, Ti, and Ca contents in the

266 experimental melts are comparable to those in the natural melts saturated in amphibole
 267 ($\text{SiO}_2 = 34.14\text{--}68.7$ wt%, $\text{TiO}_2 = 0.09\text{--}5.39$ wt%, $\text{CaO} = 1.6\text{--}12.89$ wt%; data sources in
 268 Fig. 1).

269 For the mineral composition model, we have

$$270 \quad \ln D_0^{\text{amph}} = -4.21(\pm 1.20) + \frac{7.27(\pm 0.88) \cdot 10^4}{RT} + 1.52(\pm 0.24) X_{\text{Ti}}^{\text{amph}} - 0.35(\pm 0.06) X_{\text{Mg}}^{\text{amph}} \quad (14)$$

$$- 1.83(\pm 0.34) X_{\text{Na}}^{\text{amph}} - 2.95(\pm 0.34) X_{\text{K}}^{\text{amph}},$$

$$271 \quad r_0^{\text{amph}} = 1.043(\pm 0.004) - 0.039(\pm 0.012) X_{\text{Fm}}^{\text{amph-M4}}, \quad (15)$$

$$272 \quad E^{\text{amph}} = 337(\pm 23). \quad (16)$$

273 The mineral composition model indicates REE partition coefficients in amphibole
 274 increase with the increase of Ti content and decrease with the increase of T and Mg, Na,
 275 and K contents in the amphibole. Fig. 4d shows a negative correlation between
 276 amphibole-melt Sm partition coefficient and T that is consistent with the expression for
 277 D_0 in the mineral composition model (Eq. (14)). In order to highlight the effect of
 278 amphibole composition, we subtract the effect of T on the amphibole-melt Sm partition
 279 coefficient using the following expression

$$280 \quad \overline{D}_{\text{Sm}}^{\text{amph-melt}} = D_{\text{Sm}}^{\text{amph-melt}} \exp \left[\frac{4\rho EN_A}{RT} \left(\frac{r_0}{2} (r_0 - r_{\text{Sm}})^2 - \frac{1}{3} (r_0 - r_{\text{Sm}})^3 \right) - \frac{7.27 \times 10^4}{RT} \right], \quad (17)$$

281 where $\overline{D}_{\text{Sm}}^{\text{amph-melt}}$ is the normalized amphibole-melt Sm partition coefficient; r_0 is
 282 calculated using Eq. (15) and E is that in Eq. (16). Figs. 4e, 4f, and supplementary Fig. S4
 283 show that, to the first order, normalized amphibole-melt Sm partition coefficient
 284 positively correlates with Ti content, and negatively correlates with Mg and K contents in
 285 the amphibole, consistent with Eq. (14). The negative correlation with Na contents in

286 amphibole is less clear (Fig. S4a), but it is clearer when other compositional effects are
287 subtracted from the normalized amphibole-melt Sm partition coefficient (not shown). The
288 Ti, Mg, Na, and K contents in the experimental amphiboles are comparable to those in
289 natural amphiboles ($\text{TiO}_2 = 0.73\text{--}6.35$, $\text{MgO} = 6.35\text{--}18.5$, $\text{Na}_2\text{O} = 1.20\text{--}4.04$ and $\text{K}_2\text{O} =$
290 $0.03\text{--}2.77$; data sources in Fig. 1).

291 In both the mineral and melt composition models, r_0 decreases with increasing Fm
292 content of the M4 site in the amphibole. We interpret this to indicate that the ideal radius
293 of the M4 site decreases with increasing occupancy by elements with relatively small
294 ionic radius such as Mg, Fe^{2+} , and Mn^{2+} . The range in Fm content of the M4 site in the
295 experimental amphibole is 0–0.58, which exceeds the 0–0.47 observed in the compilation
296 of natural amphiboles (data source in Fig. 1). This range in Fm content of the M4 site in
297 the compilation of natural amphiboles translates to a small range in r_0 of 1.02–1.045 Å
298 which is consistent with the subparallel parabola defined by the REE + Y partitioning
299 data (Fig. 2). Further, the proximity of r_0 to MREE such as Dy (1.027 Å) and Tb (1.04
300 Å) also explains why fractional crystallization of amphibole can produce depletion in
301 MREEs relative to HREEs and LREEs in the magma (Davidson et al., 2007; Davidson et
302 al., 2013).

303

304 **4. Discussion**

305 Our mineral composition and melt composition models reproduce the 556
306 partitioning data from the 100 partitioning experiments (fits to the individual experiments
307 are shown in Supplementary Figs. S2 and S3). The partition coefficients predicted by the
308 melt composition model (Fig. 3a) and the mineral composition model (Fig. 3b) both

309 follow the 1:1 correlation line when plotted against the measured values and generally
310 fall between the 1:2 and 2:1 correlation lines. Hence to the first approximation, both
311 models equally describe the variability of partition coefficients. In detail, the melt
312 composition model ($C_p^2 = 41.3$) performs slightly better than the mineral composition
313 model ($C_p^2 = 93.7$), especially for cases when measured $D > 1$.

314

315 **4.1. Comparison with the empirical model of Tiepolo et al. (2007)**

316 Our new melt composition model has 4 variables and 7 coefficients for the 15
317 elements (REE+Y), whereas the melt composition model of Tiepolo et al. (2007), which
318 is a linear fit to one composition variable, has 8 coefficients for 4 elements (La, Dy, Y,
319 and Yb). In terms of reproducing measured partitioning data for these 4 elements, the
320 Pearson's Chi-square for the original model of Tiepolo et al. (2007) (26.0) is larger than
321 our melt model (11.6 for a fit using La, Dy, Y, and Yb only). To further compare with the
322 model of Tiepolo et al. (2007), we recalibrated their equations for the 15 elements
323 (REE+Y) using our compiled database (Table S1 provides the new coefficients). The
324 updated model has a C_p^2 value of 54.6, which is still larger than that for our melt model
325 (41.3). Therefore, our melt composition model has a better reproducibility and a smaller
326 number of coefficients to describe the REE partitioning between amphibole and silicate
327 melt. This further underscores the advantage and importance of the lattice strain model in
328 quantifying REE partitioning in amphibole. In addition, as shown later in this study, our
329 mineral composition model provides an understanding of the REE substitution
330 mechanism in amphibole, and has the advantage of being applicable to natural samples

331 without the knowledge of the melt composition.

332

333 **4.2. Relation between the mineral composition and melt composition models**

334 The connection between the mineral composition and melt composition models
335 can be understood in terms of amphibole-melt phase equilibria. To within estimated
336 uncertainties, the coefficients in the equations for r_0 and best-fit values for E are identical
337 between the melt composition and mineral composition models (Eqs. (12) vs. (15); Eqs.
338 (13) vs. (16)). This implies that D_0 values between the two models are the same, given
339 the two models are equivalent in terms of reproducing measured REE partitioning data
340 (Figs. 3a and 3b). Equating Eqs. (11) and (14), we have the following expression relating
341 amphibole composition to coexisting melt composition,

$$342 \quad -3.08 + 0.74 \ln(X_{\text{Si}}^{\text{melt}}) - 0.33 \ln(X_{\text{Ti}}^{\text{melt}}) - 0.84 \ln(X_{\text{Ca}}^{\text{melt}}) = -4.21 + \frac{7.27 \cdot 10^4}{RT} + 1.52 X_{\text{Ti}}^{\text{amph}} - 0.35 X_{\text{Mg}}^{\text{amph}} - 1.83 X_{\text{Na}}^{\text{amph}} - 2.95 X_{\text{K}}^{\text{amph}} \quad (18)$$

344 Eq. (18), in effect, describes the liquidus of amphibole, and hence can be taken as a
345 thermometer for amphibole-melt equilibria, viz.,

$$346 \quad T = \frac{8.74 \cdot 10^3}{1.13 - 1.52 X_{\text{Ti}}^{\text{amph}} + 0.35 X_{\text{Mg}}^{\text{amph}} + 1.83 X_{\text{Na}}^{\text{amph}} + 2.95 X_{\text{K}}^{\text{amph}} + 0.74 \ln(X_{\text{Si}}^{\text{melt}}) - 0.33 \ln(X_{\text{Ti}}^{\text{melt}}) - 0.84 \ln(X_{\text{Ca}}^{\text{melt}})} \quad (19)$$

348 This thermometer provides an opportunity to independently test our melt composition
349 model (Eqs. (1) and (11)–(13)) and mineral composition model (Eqs. (1) and (14)–(16))
350 as discussed below.

351 There are a large number of amphibole-melt phase equilibria studies reported in
352 the literature. Here we use Eq. (19) to calculate the temperatures of 185 amphibole-melt

353 phase equilibrium experiments from 16 studies (Alonso-Perez et al., 2009; Blatter et al.,
354 2013; Costa et al., 2004; Foden and Green, 1992; Gardner et al., 1995; Grove et al., 1997;
355 Grove et al., 2003; Holtz et al., 2004; Kawamoto, 1996; Moore and Carmichael, 1998;
356 Nandedkar et al., 2014; Nekvasil et al., 2004; Pichavant et al., 2002; Pilet et al., 2010;
357 Prouteau and Scaillet, 2003; Sato et al., 2005). These experiments were conducted at
358 730–1130°C and 0.1–1.5 GPa, generally at lower P - T conditions compared to the REE
359 partitioning experiments. Despite some overlap in composition, these experiments
360 produced calcic amphiboles generally higher in Si and lower in alkalis, and melt with
361 higher SiO₂ content compared to those in the REE partitioning experiments (Fig. 1). The
362 temperatures of these experiments calculated using our thermometer (Eq. (19)) and the
363 measured temperatures generally follow the 1:1 correlation line to within 100°C of the
364 measured temperature with a precision of 66°C (RMSE) (Fig. 5), which is an independent
365 verification of our amphibole-melt thermometer (Eq. 19) and hence our mineral
366 composition and melt composition models. Furthermore, the validity of our thermometer
367 to lower P - T conditions and more evolved amphibole and melt composition compared to
368 the REE partitioning experiments suggests the applicability of our models at these
369 conditions.

370 Our thermometer for amphibole-melt equilibria (Eq. 19) shows similarities to a
371 recent amphibole-melt thermometer of Putirka (2016) that has the expression

$$372 \quad T(^{\circ}\text{C}) = \frac{8037.85}{3.69 + 2.62 X_{\text{H}_2\text{O}}^{\text{melt}} + 0.66 \text{Fe}_{\text{total}}^{\text{amph}} - 0.416 \ln(X_{\text{TiO}_2}^{\text{melt}}) - 0.37 \ln(X_{\text{MgO}}^{\text{melt}}) - 1.05 \ln(X_{\text{FmO}}^{\text{melt}} X_{\text{Al}_2\text{O}_3}^{\text{melt}}) - 0.462 \ln(D_{\text{Ti}})}, \quad (20)$$

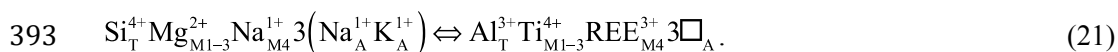
373 where X_i^{melt} are hydrous mole fractions of oxides in the melt, $\text{Fe}_{\text{total}}^{\text{amph}}$ is the total Fe cation
374 number in amphibole (per 23 oxygen), and D_{Ti} is the ratio of the Ti cation number in

375 amphibole (per 23 oxygen) divided by the hydrous mole fraction of Ti in the melt. This
376 thermometer and our thermometer both involve the temperature dependence of Ti
377 partitioning between the amphibole and melt. The thermometer of Putirka (2016) has
378 better precision (38°C) than our thermometer (66°C) based on the same data set as in Fig.
379 5, but the two thermometers are surprisingly comparable, especially given that our
380 models are calibrated to predict REE partitioning between amphibole and melt and not
381 temperatures. Therefore, our thermometer captures the essential parameters required in a
382 thermometer for amphibole-melt equilibria.

383

384 **4.3. Substitution mechanism**

385 The mineral composition model may provide insights to the REE substitution
386 mechanism in amphibole. According to the mineral composition model, D_0 positively
387 correlates with Ti and negatively with Mg. Hence REE substitution is related to the Ti–
388 Al^{iv} substitution in the M1,2,3 and tetrahedral sites. Furthermore, the model may suggest
389 that REE substitution for Na in the M4 site is charge compensated by vacancies in the A
390 site, given the negative correlation between Na and K contents in amphibole and D_0 .
391 Taken together, the mineral composition model suggests the following substitution
392 mechanism of REE in amphibole,



394 According to this substitution mechanism, REE partition coefficients should positively
395 correlate with Al^{T} similar to that observed in clinopyroxene (e.g Cascio et al., 2008;
396 Gaetani and Grove, 1995; Hill et al., 2000; Lundstrom et al., 1998; Wood and Blundy,
397 1997). There is a weak positive correlation between Al^{T} and normalized amphibole-melt

398 Sm partition coefficient (Fig. S4c), and its scatter may be due to the effect of variation in
399 other mineral compositions (e.g. Ti, Mg, Na, and K) similar to that observed for Na
400 content in the mineral composition model (Fig. S4a). A mineral composition model with
401 Al^T , Mg, Na, and K contents in the amphibole as compositional variables for D_0 has a
402 Pearson's Chi-square of 117, which is higher than our preferred mineral composition
403 model (93.7). Although Al^T plays an important role in REE substitution in amphibole, in
404 practice our mineral composition model performs slightly better when we use Ti rather
405 than Al^T as a compositional variable.

406

407

5. Applications

408

5.1. Melting of amphiboles in the mantle

409

Amphibole is often observed in mantle xenoliths brought to the surface by basalt
410 volcanism, suggesting the presence of hydrated and metasomatized mantle lithosphere
411 (e.g. Boettcher and O'Neil, 1980; Chazot et al., 1996; Ionov and Hofmann, 1995). Partial
412 melting of such mantle can give rise to melts with a range of compositions (e.g., alkali
413 basalts to nephelinites) (e.g. Médard et al., 2006; Pilet et al., 2008; Sorbadere et al.,
414 2013). In general, major element compositions in mantle amphiboles vary considerably
415 (Figs. 1d–f). According to the data compiled from 10 studies shown in Fig. 1, TiO_2 in
416 amphiboles found in mantle xenoliths varies from 0.15 to 5.94 wt%, MgO from 9.82 to
417 19.43 wt%, Na_2O from 2.31 to 4.3 wt%, and K from 0 to 2.05 wt%. Based on our mineral
418 model, we expect considerable variability in amphibole-melt REE partition coefficients.
419 For purpose of demonstration, we calculated the amphibole-melt REE partition
420 coefficients in amphiboles found in mantle xenoliths from the 10 studies listed in table 1

421 using the mineral composition model for a temperature of 1000°C. As shown in Fig. 6,
422 amphibole-melt REE partition coefficients in amphiboles found in xenoliths vary by
423 nearly an order of magnitude, purely due to their compositional variation. Further, the
424 REE partition coefficients decrease more than 20% when the temperature is increased to
425 1100°C (cf. heavy blue and red lines in Fig. 6). Despite the large range in REE partition
426 coefficient, its pattern does not noticeably change due to the small range in Fm content in
427 the M4 site of the amphiboles. This simple example demonstrates the importance of
428 composition- and temperature- dependent amphibole-melt REE partition coefficients to
429 geochemical modeling of melting of an amphibole-bearing lithology in the mantle. For
430 convenience, we list in Table 2 the average, maximum, and minimum REE partition
431 coefficients between amphiboles in mantle xenoliths and melt calculated using the
432 mineral composition model at four selected temperatures.

433

434 **5.2. Fractional crystallization of arc magmas**

435 Fractional crystallization of amphibole and clinopyroxene in arc magmas has been
436 postulated to decrease Dy/Yb and Dy/Dy* $\left(\text{Dy}_N / \left(\text{La}_N^{4/13} \text{Yb}_N^{9/13} \right) \right)$ ratios (i.e. depletion in
437 MREEs relative to HREEs and LREEs) with increasing SiO₂ content, as observed in rock
438 samples from single arc volcanoes (Davidson et al., 2007; Davidson et al., 2013).
439 However, given the large range in published mineral-melt partition coefficients, the
440 relative importance of amphibole and clinopyroxene in producing low Dy/Yb and
441 Dy/Dy* ratios in arc magmas is not clear. In order to better understand this, we use REE
442 partitioning models and mass balance calculations to estimate and compare the effects of
443 amphibole and clinopyroxene fractional crystallization on the REE patterns of

444 experimental melts compositionally similar to arc magmas (Nandedkar, 2014; Nandedkar
445 et al., 2014). The experiments of Nandedkar et al. (2014) and Nandedkar (2014) simulate
446 fractional crystallization of the same initial starting material at pressures of 0.7 GPa and
447 0.4 GPa, respectively. (Hereafter we refer to the experiments of Nandedkar et al. (2014)
448 as the 0.7 GPa experiments and those of Nandedkar (2014) as the 0.4 GPa experiments.)
449 The initial starting material in these experiments is an olivine-tholeiite with an Mg# of 73
450 and H₂O content of 3 wt%, and both experiments were run at an oxygen fugacity of Ni-
451 NiO. The experimental temperatures of the 0.7 GPa and 0.4 GPa experiments range from
452 1170 to 700°C and 1110 to 920°C, respectively. The final amounts of fractional
453 crystallization are 85 wt% for the 0.7 GPa experiments and 76 wt% for the 0.4 GPa
454 experiments. Both experiments crystallized clinopyroxene, olivine, plagioclase, and
455 magnetite, but the 0.7 GPa experiment also crystallized amphibole with less plagioclase.
456 This may be due to the greater stability of amphibole and the lesser stability of
457 plagioclase at high pressure (Allen and Boettcher, 1983; Nandedkar, 2014; Spulber and
458 Rutherford, 1983). Hence, the comparison between the model REE patterns and
459 abundances in the melts of these experiments using REE partitioning models and mass
460 balance calculations provide an insight into the effect of fractional crystallization on the
461 REE pattern of arc magmas under different *P-T* conditions and crystallizing phases.
462 Particularly interesting is the effect of amphibole fractional crystallization, which may
463 play a key role in the depletion of MREEs relative to HREEs in arc magmas (Davidson et
464 al., 2007; Davidson et al., 2013).

465 We used the temperature, mineral and melt composition in the 0.7 GPa and 0.4
466 GPa experiments to calculate the amphibole-melt and clinopyroxene-melt REE partition

467 coefficients using the melt composition model of this study and the model of Sun and
468 Liang (2012). The amphibole-melt REE partition coefficients in the 0.7 GPa experiments
469 were measured by Nandedkar et al. (2016), and they are part of the partitioning data used
470 for our model calibration. However, we chose to use our models to calculate the
471 amphibole-melt REE partition coefficients to understand what parameters cause changes
472 in the partition coefficients between different experimental runs. The calculated
473 amphibole-melt MREE and HREE partition coefficients in the 0.7 GPa experiments
474 increase by approximately an order of magnitude from the highest to lowest temperature
475 experiment due to the increase in Si, and decrease in Ti and Ca content in the melt (Fig.
476 7a). In contrast to the MREE and HREE, the LREE partition coefficients do not vary
477 significantly because elements with larger ionic radius relative to r_0 become more
478 incompatible with decreasing temperature (Eq. 1), and this counteracts the increase in D_0 .
479 A calculation using the mineral composition model from this study also predicts an
480 increase in MREE and HREE partition coefficients with progressive fractional
481 crystallization largely due to the decrease in temperature, but also due to the decrease in
482 Na and K content in the amphibole. However, the increase of partition coefficients is a
483 factor of 2 smaller than that predicted by the melt composition model at 730°C. The
484 disagreement between the models is likely due to the low crystallization temperature
485 (730°C), which is below the model calibration range (780–1100°C). (The amphibole
486 formed at 730°C is cummingtonite unlike the magnesio-hornblende formed at slightly
487 higher temperature of 780°C, which may give rise to a different REE substitution
488 mechanism than those described in section 4.3. We suspect kinetics may also play a role
489 in controlling major element compositions in amphiboles at lower temperatures). Hence

490 caution should be exercised when extrapolating our models to T - X conditions outside the
491 calibration range (Table 1). At temperatures higher than 730°C, the differences between
492 the amphibole-melt REE partition coefficients predicted by the two models are all within
493 34%, and the results discussed in the rest of this section are not model dependent. The
494 range in clinopyroxene-melt REE partition coefficients in the 0.7 GPa and 0.4 GPa
495 experiments are similar to each other except for the high Al clinopyroxene found in the
496 0.7 GPa experiment at 1040°C. The olivine-melt, opx-melt, and plagioclase-melt REE
497 partition coefficients are calculated using the models of Sun and Liang (2013b), Yao et al.
498 (2012), and Sun et al. (2017) respectively. The spinel-melt REE partition coefficients are
499 from Kelemen et al. (2003). The other phases such as apatite and magnetite were not
500 considered for simplicity.

501 The partition coefficients and the phase proportions in the 0.7 GPa and 0.4 GPa
502 experiments (Nandedkar, 2014; Nandedkar et al., 2014) were used to model the REE
503 abundances in the melts during fractional crystallization. The model results are shown in
504 in Figs. 7b, c, and d. The Dy/Dy* and Dy/Yb ratios of the 0.7 GPa melt decrease
505 significantly more than those of the 0.4 GPa melt during fractional crystallization (Fig.
506 7b). Furthermore, the 0.7 GPa melts are more depleted in MREEs and HREEs compared
507 to the 0.4 GPa melts for a given degree of fractional crystallization (Figs. 7c and d).
508 These differences are due to fractional crystallization of amphibole in the 0.7 GPa melts.
509 As shown in the results section, amphibole fractional crystallization decreases the
510 Dy/Dy* and Dy/Yb ratios in the melt due to the affinity of amphibole for MREEs over
511 HREEs and LREEs (i.e. similarity between r_0 of the amphibole and ionic radius of
512 MREEs) (Figs. 2 and 7a). In addition, amphibole fractional crystallization moderates the

513 MREE and HREE concentration in the melt since they behave compatibly in amphiboles,
514 especially in those crystallizing from more evolved melts (i.e., high Si) at lower
515 temperatures (Fig. 7a). In contrast, the Dy/Dy* and Dy/Yb ratios do not decrease as much
516 and the MREE and HREE concentrations are significantly higher in the 0.4 GPa melts
517 than the 0.7 GPa melts since they do not crystallize amphibole (Fig. 7b). To some extent,
518 the Dy/Dy* and Dy/Yb ratios in the 0.4 GPa melts decrease due to clinopyroxene
519 fractional crystallization (Fig. 7b), but by much less than the 0.7 GPa melts, since REEs
520 are incompatible in the crystallizing clinopyroxenes especially at high temperatures (Fig.
521 7a). In contrast, amphibole can significantly fractionate the REE pattern of the 0.7 GPa
522 melts due to the lower crystallization temperatures in the 0.7 GPa melts compared to the
523 0.4 GPa melts for a given degree of fractional crystallization, perhaps due to the larger
524 temperature difference between the solidus and liquidus at higher pressure.

525 Applying the present REE partitioning model (melt composition model) to the 0.7
526 GPa experiments by Nandedkar et al. (2014) suggests that the amphibole-melt REE
527 partition coefficient can vary by an order of magnitude during fractional crystallization of
528 an arc magma due to changes in T , and the melt and amphibole compositions. This range
529 of values demonstrates the importance of composition- and temperature-dependent REE
530 partition coefficients in geochemical modeling of amphibole-melt fractionation. For
531 convenience, we list the amphibole-melt REE partition coefficients for amphiboles in the
532 0.7 GPa experiments calculated using the melt composition model (Table 3). Our
533 modeling results suggest that fractional crystallization of amphibole plays a key role in
534 decreasing the Dy/Yb and Dy/Dy* ratios and also in moderating the MREE and HREE
535 concentrations in arc magmas. Fractional crystallization of clinopyroxene can also

536 decrease the Dy/Yb and Dy/Dy* ratios in the arc magmas, although much less efficiently.
537 The pressure of fractional crystallization affects the crystallization temperature of the
538 melt and stability of amphibole (Allen and Boettcher, 1983; Nandedkar, 2014; Spulber
539 and Rutherford, 1983), so it is also a key factor that controls the behavior of REE in
540 solidifying magmas.

541 Our model results suggest that arc magmas that crystallize amphibole should have
542 a fairly restricted range in MREE and HREE concentrations and low Dy/Yb and Dy/Dy*
543 ratios compared to those that do not crystallize amphibole (Fig. 7). As an example of
544 geological application, we compare two sets of samples from single arc volcanoes, one in
545 which these characteristics are present and another in which they are not. Samples from
546 Mt. Pelée in the Lesser Antilles Arc (Davidson and Wilson, 2011) (Fig. 8a) show the
547 effects of fractional crystallization of amphibole, while those from Anatahan Island in the
548 Mariana Arc (Wade et al., 2005) (Fig. 8b) do not. The samples from Mt. Pelée have a
549 fairly restricted range in MREE and HREE concentrations compared to those from
550 Anatahan Island despite the similar range in bulk SiO₂ content (51–63 wt% for Mt. Pelée
551 and 49–66 wt% for Anatahan Island) and other major element contents (Fig. S5)
552 suggesting similar range in degrees of fractional crystallization between the two sets of
553 samples. To the first order, REE and Y concentrations in the samples from Mt. Pelée and
554 Anatahan Island can be fairly well reproduced using the model REE and Y
555 concentrations in subsets of the 0.7 GPa experiments (Nandedkar et al., 2014) and 0.4
556 GPa experiments (Nandedkar, 2014) that have the most similar major element
557 concentrations to those in the samples (Fig. S5) and assuming the REE and Y
558 concentrations in the initial melts are those in the samples with lowest SiO₂ contents. The

559 model REE and Y concentrations also reproduce the greater decrease in Dy/Dy* and
560 Dy/Yb ratios in the samples from Mt. Pelée compared to those from Anatahan Island
561 (Figs. 8c and d). Although scatter in the data (Fig. 8c and d) and variation in the isotopic
562 composition may suggest some amount of source variation and/or crustal contamination
563 (Davidson and Wilson, 2011), the model results suggest amphibole fractional
564 crystallization associated with Mt. Pelée samples but not the Anatahan Island samples.
565 The *P-T-X* conditions of the equilibrium crystallization experiments designed for
566 studying the Mt. Pelée samples (Martel et al., 1998; Martel et al., 1999; Pichavant et al.,
567 2002) are a more accurate representation of those in the Mt. Pelée magma chamber, but
568 we chose to use the 0.7 GPa experiments (Nandedkar et al., 2014) as they are fractional
569 crystallization experiments that allows continuous modeling of the effects of changing
570 temperature and melt/mineral composition on the REE concentration in a crystallizing
571 melt. A combination of fractional crystallization experiments ran at relevant *P-T-X*
572 conditions and the REE partitioning models for amphibole and other mineral phases
573 (Dyger et al., 2014; Sun et al., 2017; Sun and Liang, 2012; Sun and Liang, 2013b; Yao et
574 al., 2012) may be useful for unraveling the *P-T* conditions and variations in major and
575 REE abundance of sets of samples from single arc volcanoes.

576

577

6. Conclusions

578 The partitioning of rare earth elements between amphibole and silicate melt
579 depends on temperature, and amphibole and melt compositions. We developed two
580 parameterized lattice strain models for REE and Y partitioning between amphibole and
581 silicate melt over a large range of *P-T-X* using published partitioning data between

582 amphibole and silicate melt and non-linear least squares regression method. The melt
583 composition model suggests that REE and Y partition coefficients in amphibole
584 positively correlate with Si content, and negatively correlate with Ti and Ca contents in
585 the melt. The mineral composition model suggests that REE and Y partition coefficients
586 in amphibole negatively correlate with T and Mg, Na, and K contents and positively
587 correlate with Ti content in amphibole. In both the mineral and melt composition models,
588 r_0 negatively correlates with the Fm content in the M4 site of amphibole and E is a
589 constant. The very similar coefficients of the equations for r_0 and best-fit values for E in
590 the two models suggest that the D_0 in the two models are equivalent. Hence there are
591 considerable trade-offs between major element compositions of coexisting amphibole and
592 melt in the parameterized lattice strain models for REE partitioning in amphibole. The
593 connection is the liquidus surface of amphibole. To further demonstrate this point, we
594 developed a hybrid model for amphibole-melt REE partitioning using a combination of
595 amphibole and melt compositions and the results are summarized in Appendix A. The
596 hybrid model, which performs slightly better than the melt composition model and the
597 mineral composition model, can be used to predict REE partition coefficients if major
598 element compositions of both amphibole and melt are available.

599 Application of our mineral composition model to amphiboles found in mantle
600 xenoliths suggests an order of magnitude variation in the amphibole-melt REE partition
601 coefficients purely due to compositional variation. Application of our melt composition
602 model to fractional crystallization experiments of arc magma (Nandedkar, 2014;
603 Nandedkar et al., 2014) suggests that REE partition coefficients between amphibole and
604 melt can increase by an order of magnitude due to a combined effect of decreasing T and

605 varying amphibole (e.g. decrease in Na and K) and melt compositions (e.g. increase in Si)
606 within this environment. In contrast, r_0 of the crystallizing amphiboles does not change
607 significantly and remains similar to the ionic radius of MREE such as Dy and Tb.
608 Therefore, fractional crystallization of amphibole can play a key role in buffering the
609 REE concentrations in arc magmas, and also in depleting its MREEs relative to HREEs
610 and LREEs.

611

612

7. Implications

613 Our new mineral composition model is a useful tool to estimate the REE and Y
614 concentration in silicate melt that is in equilibrium with amphibole. Previous models of
615 amphibole-melt REE partition coefficients (Hilyard et al., 2000; Sisson, 1994; Tiepolo et
616 al., 2007; Tiepolo et al., 2000) require the major element composition of the melt that is
617 in equilibrium with amphibole, which is not always available for natural samples such as
618 cumulates. Studies on amphibole-bearing rocks (e.g. Davidson and Wilson, 2011; Peters
619 et al., 2017) had to choose a set of amphibole-melt trace element partition coefficients
620 from the literature to estimate the trace element concentration in the equilibrium melt.
621 The new mineral composition model developed in the present study is useful in such
622 instances as it only requires the amphibole composition (i.e. Ti, Mg, Na, and K contents)
623 and temperature. Here temperature can be estimated using the amphibole composition-
624 dependent thermometer of Putirka (2016). The application of the mineral composition
625 model on amphibole-bearing cumulates would allow estimation of the REE concentration
626 in the melt that is in equilibrium with the amphibole-bearing cumulate, which is a useful
627 information for understanding the origin of the cumulates and the effect of its

628 crystallization on evolution of the trace element concentration in the melt. It can also be
629 used to model processes such as formation of amphibole by reaction-replacement of
630 clinopyroxene observed in cumulates (Smith, 2014), which may be an important process
631 for explaining the rarity of amphibole phenocrysts in arc lavas i.e. amphibole being a
632 ‘cryptic’ fractionating phase (Davidson et al., 2007).

633 Applications of the new amphibole-melt REE partitioning models demonstrate the
634 significantly stronger effect of amphibole fractional crystallization, relative to
635 clinopyroxene fractional crystallization, on buffering the MREE and HREE
636 concentrations and decreasing Dy/Yb and Dy/Dy* ratios in arc magmas (Davidson et al.,
637 2007; Davidson et al., 2013). The magnitude of decrease in Dy/Yb and Dy/Dy* ratios
638 found in the samples from Mt. Pelée consistent with amphibole fractional crystallization,
639 is also observed in many other sets of samples from single arc volcanoes (Fig. 7 in
640 Davidson et al., 2013). This suggests that fractional crystallization of amphibole in arc
641 magmas is a common process, which is consistent with its common observation in arc
642 cumulates (e.g. Beard, 1986; DeBari and Coleman, 1989; Jagoutz et al., 2009; Lapierre et
643 al., 1992; Larocque and Canil, 2010). Our study implies that REEs are especially
644 enriched in amphibole-rich cumulates that crystallize from the most differentiated arc
645 magmas, since amphibole-melt REE partition coefficient increases with increasing
646 differentiation of arc magmas.

647

648 **Appendix A.** A Hybrid Model for Amphibole-Melt REE Partitioning

649 Following the same procedure outlined in the parameterization method, we found a
650 hybrid model in which parameters D_0 , r_0 , and E take on the following expressions:

651
$$\ln D_0^{\text{amph}} = -3.17(\pm 0.71) - 0.61(\pm 0.10)X_{\text{Si}}^{\text{amph}} - 2.19(\pm 0.20)X_{\text{Na}}^{\text{amph}} - 1.95(\pm 0.32)X_{\text{K}}^{\text{amph}} + 0.89(\pm 0.29)\ln(X_{\text{Si}}^{\text{melt}}) - 1.21(\pm 0.07)\ln(X_{\text{Ca}}^{\text{melt}}), \quad (\text{A1})$$

652
$$r_0^{\text{amph}} = 1.044(\pm 0.002) - 0.050(\pm 0.008)X_{\text{Fm}}^{\text{amph-M4}}, \quad (\text{A2})$$

653
$$E^{\text{amph}} = 332(\pm 15), \quad (\text{A3})$$

654 where r_0 is in Å; and E is in GPa; and numbers in parentheses are 2σ uncertainties
655 estimated directly from the simultaneous inversion. The hybrid model has 9 fitting
656 parameters and provides an improved fit ($C_p^2 = 31.5$) over the melt (7 fitting parameters)
657 and mineral composition (9 fitting parameters) models presented in the main text. It can
658 be used to predict REE partition coefficients if major element compositions of both
659 amphibole and melt composition are available.

660

661 **Acknowledgements**

662 We thank Othmar Müntener for useful discussion and for sharing amphibole-melt
663 partitioning data. This paper is benefited from thoughtful review comments by Stefan
664 Peters and Calvin Barnes. This work was supported by NSF grants OCE-1355932 and
665 EAR-0810191 (to A.E.S.) and EAR-1624516 (to Y.L.), and a Dissertation Fellowship at
666 Brown University (to K.S.).

667

668 **References**

- 669 Adam, J., and Green, T.H. (1994) The effects of pressure and temperature on the
670 partitioning of Ti, Sr and REE between amphibole, clinopyroxene and basanitic
671 melts. *Chemical Geology*, 117(1), 219-233.
- 672 Adam, J., and Green, T.H. (2003) The influence of pressure, mineral composition and
673 water on trace element partitioning between clinopyroxene, amphibole and
674 basanitic melts. *European Journal of Mineralogy*, 15(5), 831-841.

- 675 Adam, J., and Green, T.H. (2006) Trace element partitioning between mica-and
676 amphibole-bearing garnet lherzolite and hydrous basanitic melt: 1. Experimental
677 results and the investigation of controls on partitioning behaviour. Contributions
678 to Mineralogy and Petrology, 152(1), 1-17.
- 679 Allen, J.C., and Boettcher, A.L. (1983) The stability of amphibole in andesite and basalt
680 at high pressures. American Mineralogist, 68(3-4), 307-314.
- 681 Alonso-Perez, R., Müntener, O., and Ulmer, P. (2009) Igneous garnet and amphibole
682 fractionation in the roots of island arcs: experimental constraints on andesitic
683 liquids. Contributions to Mineralogy and Petrology, 157(4), 541-558.
- 684 Ballhaus, C. (1993) Redox states of lithospheric and asthenospheric upper mantle.
685 Contributions to Mineralogy and Petrology, 114(3), 331-348.
- 686 Beard, J.S. (1986) Characteristic mineralogy of arc-related cumulate gabbros:
687 implications for the tectonic setting of gabbroic plutons and for andesite genesis.
688 Geology, 14(10), 848-851.
- 689 Bernard, A., Knittel, U., Weber, B., Weis, D., Albrecht, A., Hattori, K., Klein, J., and
690 Oles, D. (1996) Petrology and geochemistry of the 1991 eruption products of
691 Mount Pinatubo. In R.S. Punongbayan, and C.G. Newhall, Eds. Fire and mud:
692 eruptions and lahars of Mount Pinatubo, Philippines, p. 767-797. University of
693 Washington Press, Seattle.
- 694 Blatter, D.L., Sisson, T.W., and Hankins, W.B. (2013) Crystallization of oxidized,
695 moderately hydrous arc basalt at mid- to lower-crustal pressures: implications for
696 andesite genesis. Contributions to Mineralogy and Petrology, 166(3), 861-886.
- 697 Blundy, J., and Wood, B. (1994) Prediction of crystal melt partition coefficients from
698 elastic moduli. Nature, 372, 452-454.
- 699 Boettcher, A.L., and O'Neil, J.R. (1980) Stable isotope, chemical, and petrographic
700 studies of high-pressure amphiboles and micas: evidence for metasomatism in the
701 mantle source regions of alkali basalts and kimberlites. American Journal of
702 Science, 280-A, 594-621.
- 703 Bottazzi, P., Tiepolo, M., Vannucci, R., Zanetti, A., Brumm, R., Foley, S.F., and Oberti,
704 R. (1999) Distinct site preferences for heavy and light REE in amphibole and the
705 prediction of $^{Amph/L}D_{REE}$. Contributions to Mineralogy and Petrology, 137(1-2),
706 36-45.
- 707 Brenan, J.M., Shaw, H.F., Ryerson, F.J., and Phinney, D.L. (1995) Experimental
708 determination of trace-element partitioning between pargasite and a synthetic
709 hydrous andesitic melt. Earth and Planetary Science Letters, 135(1), 1-11.
- 710 Brice, J.C. (1975) Some thermodynamic aspects of the growth of strained crystals.
711 Journal of Crystal Growth, 28(2), 249-253.

- 712 Brophy, J.G. (2008) A study of rare earth element (REE)–SiO₂ variations in felsic liquids
713 generated by basalt fractionation and amphibolite melting: a potential test for
714 discriminating between the two different processes. *Contributions to Mineralogy
715 and Petrology*, 156(3), 337-357.
- 716 Buckley, V.J.E., Sparks, R.S.J., and Wood, B.J. (2006) Hornblende dehydration reactions
717 during magma ascent at Soufrière Hills Volcano, Montserrat. *Contributions to
718 Mineralogy and Petrology*, 151(2), 121-140.
- 719 Cascio, M.L., Liang, Y., Shimizu, N., and Hess, P.C. (2008) An experimental study of
720 the grain-scale processes of peridotite melting: implications for major and trace
721 element distribution during equilibrium and disequilibrium melting. *Contributions
722 to Mineralogy and Petrology*, 156(1), 87-102.
- 723 Chazot, G., Charpentier, S., Kornprobst, J., Vannucci, R., and Luais, B. (2005)
724 Lithospheric mantle evolution during continental break-up: the West Iberia non-
725 volcanic passive margin. *Journal of Petrology*, 46(12), 2527-2568.
- 726 Chazot, G., Menzies, M.A., and Harte, B. (1996) Determination of partition coefficients
727 between apatite, clinopyroxene, amphibole, and melt in natural spinel lherzolites
728 from Yemen: implications for wet melting of the lithospheric mantle. *Geochimica
729 et Cosmochimica Acta*, 60(3), 423-437.
- 730 Costa, F., and Chakraborty, S. (2004) Decadal time gaps between mafic intrusion and
731 silicic eruption obtained from chemical zoning patterns in olivine. *Earth and
732 Planetary Science Letters*, 227(3), 517-530.
- 733 Costa, F., Scaillet, B., and Pichavant, M. (2004) Petrological and Experimental
734 Constraints on the Pre-eruption Conditions of Holocene Dacite from Volcan San
735 Pedro(36°S, Chilean Andes) and the Importance of Sulphur in Silicic Subduction-
736 related Magmas. *Journal of Petrology*, 45(4), 855-881.
- 737 Dalpé, C., and Baker, D.R. (2000) Experimental investigation of large-ion-lithophile-
738 element-, high-field-strength-element-and rare-earth-element-partitioning between
739 calcic amphibole and basaltic melt: the effects of pressure and oxygen fugacity.
740 *Contributions to Mineralogy and Petrology*, 140(2), 233-250.
- 741 Davidson, J., Turner, S., Handley, H., Macpherson, C., and Dosseto, A. (2007)
742 Amphibole "sponge" in arc crust? *Geology*, 35(9), 787-790.
- 743 Davidson, J., Turner, S., and Plank, T. (2013) Dy/Dy*: Variations Arising from Mantle
744 Sources and Petrogenetic Processes. *Journal of Petrology*, 54(3), 525-537.
- 745 Davidson, J., and Wilson, M. (2011) Differentiation and source processes at Mt Pelée and
746 the Quill; active volcanoes in the Lesser Antilles Arc. *Journal of Petrology*, 52(7-
747 8), 1493-1531.

- 748 DeBari, S.M., and Coleman, R. (1989) Examination of the deep levels of an island arc:
749 Evidence from the Tonsina Ultramafic - Mafic Assemblage, Tonsina, Alaska.
750 *Journal of Geophysical Research: Solid Earth*, 94(B4), 4373-4391.
- 751 Demény, A., Vennemann, T.W., Hegner, E., Ahijado, A., Casillas, R., Nagy, G.,
752 Homonnay, Z., Gutierrez, M., and Szabó, C. (2004) H, O, Sr, Nd, and Pb isotopic
753 evidence for recycled oceanic crust in the Transitional Volcanic Group of
754 Fuerteventura, Canary Islands, Spain. *Chemical Geology*, 205(1), 37-54.
- 755 Dygert, N., Liang, Y., Sun, C., and Hess, P. (2014) An experimental study of trace
756 element partitioning between augite and Fe-rich basalts. *Geochimica et*
757 *Cosmochimica Acta*, 132, 170-186.
- 758 Foden, J.D., and Green, D.H. (1992) Possible role of amphibole in the origin of andesite:
759 some experimental and natural evidence. *Contributions to Mineralogy and*
760 *Petrology*, 109(4), 479-493.
- 761 Gaetani, G.A., and Grove, T.L. (1995) Partitioning of rare earth elements between
762 clinopyroxene and silicate melt Crystal-chemical controls. *Geochimica et*
763 *Cosmochimica Acta*, 59(10), 1951-1962.
- 764 Gardner, J.E., Rutherford, M., Carey, S., and Sigurdsson, H. (1995) Experimental
765 constraints on pre-eruptive water contents and changing magma storage prior to
766 explosive eruptions of Mount St Helens volcano. *Bulletin of Volcanology*, 57(1),
767 1-17.
- 768 Gourgaud, A., Fichaut, M., and Joron, J.L. (1989) Magmatology of Mt. Pelée
769 (Martinique, FWI). I: Magma mixing and triggering of the 1902 and 1929 Pelean
770 nuées ardentes. *Journal of Volcanology and Geothermal Research*, 38(1), 143-
771 169.
- 772 Green, T.H., and Pearson, N.J. (1985) Experimental determination of REE partition
773 coefficients between amphibole and basaltic to andesitic liquids at high pressure.
774 *Geochimica et Cosmochimica Acta*, 49(6), 1465-1468.
- 775 Grégoire, M., Moine, B.N., O'Reilly, S.Y., Cottin, J.Y., and Giret, A. (2000) Trace
776 element residence and partitioning in mantle xenoliths metasomatized by highly
777 alkaline, silicate- and carbonate-rich melts (Kerguelen Islands, Indian Ocean).
778 *Journal of Petrology*, 41(4), 477-509.
- 779 Grove, T.L., Baker, M.B., Price, R.C., Parman, S.W., Elkins-Tanton, L.T., Chatterjee, N.,
780 and Müntener, O. (2005) Magnesian andesite and dacite lavas from Mt. Shasta,
781 northern California: products of fractional crystallization of H₂O-rich mantle
782 melts. *Contributions to Mineralogy and Petrology*, 148(5), 542-565.
- 783 Grove, T.L., Donnelly-Nolan, J.M., and Housh, T. (1997) Magmatic processes that
784 generated the rhyolite of Glass Mountain, Medicine Lake volcano, N. California.
785 *Contributions to Mineralogy and Petrology*, 127(3), 205-223.

- 786 Grove, T.L., Elkins-Tanton, L.T., Parman, S.W., Chatterjee, N., Müntener, O., and
787 Gaetani, G.A. (2003) Fractional crystallization and mantle-melting controls on
788 calc-alkaline differentiation trends. *Contributions to Mineralogy and Petrology*,
789 145(5), 515-533.
- 790 Hawthorne, F.C. (1983) The crystal chemistry of the amphiboles. *Canadian Mineralogist*,
791 2(2), 173-480.
- 792 Heliker, C. (1995) Inclusions in Mount St. Helens dacite erupted from 1980 through
793 1983. *Journal of Volcanology and Geothermal Research*, 66(1), 115-135.
- 794 Hill, E., Wood, B.J., and Blundy, J.D. (2000) The effect of Ca-Tschermaks component on
795 trace element partitioning between clinopyroxene and silicate melt. *Lithos*, 53(3),
796 203-215.
- 797 Hilyard, M., Nielsen, R.L., Beard, J.S., Patinõ-Douce, A., and Blencoe, J. (2000)
798 Experimental determination of the partitioning behavior of rare earth and high
799 field strength elements between pargasitic amphibole and natural silicate melts.
800 *Geochimica et Cosmochimica Acta*, 64(6), 1103-1120.
- 801 Holtz, F., Sato, H., Lewis, J., Behrens, H., and Nakada, S. (2004) Experimental Petrology
802 of the 1991-1995 Unzen Dacite, Japan. Part I: Phase Relations, Phase
803 Composition and Pre-eruptive Conditions. *Journal of Petrology*, 46(2), 319.
- 804 Ionov, D.A., and Hofmann, A.W. (1995) Nb-Ta-rich mantle amphiboles and micas:
805 Implications for subduction-related metasomatic trace element fractionations.
806 *Earth and Planetary Science Letters*, 131(3), 341-356.
- 807 Jagoutz, O.E., Burg, J.-P., Hussain, S., Dawood, H., Pettke, T., Iizuka, T., and
808 Maruyama, S. (2009) Construction of the granitoid crust of an island arc part I:
809 geochronological and geochemical constraints from the plutonic Kohistan (NW
810 Pakistan). *Contributions to Mineralogy and Petrology*, 158(6), 739.
- 811 Kawamoto, T. (1996) Experimental constraints on differentiation and H₂O abundance of
812 calc-alkaline magmas. *Earth and Planetary Science Letters*, 144(3-4), 577-589.
- 813 Kelemen, P.B., Yogodzinski, G.M., and Scholl, D.W. (2003) Along-Strike Variation in
814 the Aleutian Island Arc: Genesis of High Mg# Andesite and Implications for
815 Continental Crust. *Inside the subduction factory*, 223-276.
- 816 Kelley, K.A., and Cottrell, E. (2009) Water and the oxidation state of subduction zone
817 magmas. *Science*, 325(5940), 605-607.
- 818 Klein, M., Stosch, H.-G., and Seck, H. (1997) Partitioning of high field-strength and rare-
819 earth elements between amphibole and quartz-dioritic to tonalitic melts: an
820 experimental study. *Chemical Geology*, 138(3), 257-271.

- 821 Lapierre, H., Ortiz, L.E., Abouchami, W., Monod, O., Coulon, C., and Zimmermann, J.-
822 L. (1992) A crustal section of an intra-oceanic island arc: The Late Jurassic-Early
823 Cretaceous Guanajuato magmatic sequence, central Mexico. *Earth and Planetary*
824 *Science Letters*, 108(1-3), 61-77.
- 825 Larocque, J., and Canil, D. (2010) The role of amphibole in the evolution of arc magmas
826 and crust: the case from the Jurassic Bonanza arc section, Vancouver Island,
827 Canada. *Contributions to Mineralogy and Petrology*, 159(4), 475-492.
- 828 LaTourrette, T., Hervig, R.L., and Holloway, J.R. (1995) Trace element partitioning
829 between amphibole, phlogopite, and basanite melt. *Earth and Planetary Science*
830 *Letters*, 135(1), 13-30.
- 831 Leake, B.E., Woolley, A.R., Arps, C.E., Birch, W.D., Gilbert, C.M., Grice, J.D.,
832 Hawthorne, F.C., Kato, A., Kisch, H.J., Krivovichev, V.G., Linthout, K., Laird,
833 J.O., Mandarino, J.A., Maresch, W.V., Nickel, E.H., Rock, N.M., C, S.J., Smith,
834 D.C., Stephenson, N.C., Ungaretti, L., Whittaker, E.J., and Youzhi, G. (1997)
835 Nomenclature of amphiboles: report of the subcommittee on amphiboles of the
836 International Mineralogical Association, Commission on New Minerals and
837 Mineral Names. *Canadian Mineralogist*, 35(1), 219-246.
- 838 Lundstrom, C.C., Shaw, H.F., Ryerson, F.J., Williams, Q., and Gill, J. (1998) Crystal
839 chemical control of clinopyroxene-melt partitioning in the Di-Ab-An system:
840 implications for elemental fractionations in the depleted mantle. *Geochimica et*
841 *Cosmochimica Acta*, 62(16), 2849-2862.
- 842 Martel, C., Pichavant, M., Bourdier, J.-L., Traineau, H., Holtz, F., and Scaillet, B. (1998)
843 Magma storage conditions and control of eruption regime in silicic volcanoes:
844 experimental evidence from Mt. Pelée. *Earth and Planetary Science Letters*,
845 156(1), 89-99.
- 846 Martel, C., Pichavant, M., Holtz, F., Scaillet, B., Bourdier, J.-L., and Traineau, H. (1999)
847 Effects of f_{O_2} and H_2O on andesite phase relations between 2 and 4 kbar. *Journal*
848 *of Geophysical Research: Solid Earth*, 104(B12), 29,453-29,470.
- 849 Mayer, B., Jung, S., Romer, R.L., Stracke, A., Haase, K.M., and Garbe-Schönberg, C.D.
850 (2013) Petrogenesis of Tertiary hornblende-bearing lavas in the Rhön, Germany.
851 *Journal of Petrology*, 54(10), 2095-2123.
- 852 McDonough, W.F., and Sun, S.S. (1995) The Composition of the Earth. *Chemical*
853 *Geology*, 120(3-4), 223-253.
- 854 Médard, E., Schmidt, M.W., Schiano, P., and Ottolini, L. (2006) Melting of amphibole-
855 bearing wehrlites: an experimental study on the origin of ultra-calcic nepheline-
856 normative melts. *Journal of Petrology*, 47(3), 481-504.
- 857 Moine, B., Grégoire, M., O'Reilly, S., Sheppard, S., and Cottin, J. (2001) High field
858 strength element fractionation in the upper mantle: evidence from amphibole-rich

- 859 composite mantle xenoliths from the Kerguelen Islands (Indian Ocean). *Journal of*
860 *Petrology*, 42(11), 2145-2167.
- 861 Moore, G., and Carmichael, I.S.E. (1998) The hydrous phase equilibria (to 3 kbar) of an
862 andesite and basaltic andesite from western Mexico: constraints on water content
863 and conditions of phenocryst growth. *Contributions to Mineralogy and Petrology*,
864 130(3-4), 304-319.
- 865 Mortazavi, M., and Sparks, R.S.J. (2004) Origin of rhyolite and rhyodacite lavas and
866 associated mafic inclusions of Cape Akrotiri, Santorini: the role of wet basalt in
867 generating calcalkaline silicic magmas. *Contributions to Mineralogy and*
868 *Petrology*, 146(4), 397-413.
- 869 Nandedkar, R.H. (2014) Evolution of hydrous mantle-derived calc-alkaline liquids by
870 fractional crystallization at 0.7 and 0.4 GPa-an experimental study. Diss.,
871 Eidgenössische Technische Hochschule ETH Zürich, Nr. 21411, 2014.
- 872 Nandedkar, R.H., Hürlimann, N., Ulmer, P., and Müntener, O. (2016) Amphibole–melt
873 trace element partitioning of fractionating calc-alkaline magmas in the lower
874 crust: an experimental study. *Contributions to Mineralogy and Petrology*, 171(8-
875 9), 71.
- 876 Nandedkar, R.H., Ulmer, P., and Müntener, O. (2014) Fractional crystallization of
877 primitive, hydrous arc magmas: an experimental study at 0.7 GPa. *Contributions*
878 *to Mineralogy and Petrology*, 167(6).
- 879 Nekvasil, H., Dondolini, A., Horn, J., Filiberto, J., Long, H., and Lindsley, D.H. (2004)
880 The origin and evolution of silica-saturated alkalic suites: an experimental study.
881 *Journal of Petrology*, 45(4), 693-721.
- 882 Neumann, E.R., Wulff-Pedersen, E., Simonsen, S.L., Pearson, N.J., Martí, J., and
883 Mitjavila, J. (1999) Evidence for fractional crystallization of periodically refilled
884 magma chambers in Tenerife, Canary Islands. *Journal of Petrology*, 40(7), 1089-
885 1123.
- 886 Nicholls, I.A., and Harris, K.L. (1980) Experimental rare earth element partition
887 coefficients for garnet, clinopyroxene and amphibole coexisting with andesitic
888 and basaltic liquids. *Geochimica et Cosmochimica Acta*, 44(2), 287-308.
- 889 Nielsen, R.L. (1985) A method for the elimination of the compositional dependence of
890 trace element distribution coefficients. *Geochimica et Cosmochimica Acta*, 49(8),
891 1775-1779.
- 892 Nye, C.J., and Turner, D.L. (1990) Petrology, geochemistry, and age of the Spurr
893 volcanic complex, eastern Aleutian arc. *Bulletin of Volcanology*, 52(3), 205-226.
- 894 Pallister, J.S., Hoblitt, R.P., Meeker, G.P., Knight, R.J., and Siems, D.F. (1996) Magma
895 mixing at Mount Pinatubo: petrographic and chemical evidence from the 1991

- 896 deposits. In R.S. Punongbayan, and C.G. Newhall, Eds. Fire and mud: eruptions
897 and lahars of Mount Pinatubo, Philippines, p. 687-731. University of Washington
898 Press, Seattle.
- 899 Pallister, J.S., Thornber, C.R., Cashman, K.V., Clynne, M.A., LOWERS, H.A.,
900 Mandeville, C.W., Brownfield, I.K., and Meeker, G.P. (2008) Petrology of the
901 2004-2006 Mount St. Helens lava dome-implications for magmatic plumbing and
902 eruption triggering. US Geological Survey professional paper(1750), 647-702.
- 903 Parkinson, I.J., and Arculus, R.J. (1999) The redox state of subduction zones: insights
904 from arc-peridotites. *Chemical Geology*, 160(4), 409-423.
- 905 Peters, S.T., Troll, V.R., Weis, F.A., Dallai, L., Chadwick, J.P., and Schulz, B. (2017)
906 Amphibole megacrysts as a probe into the deep plumbing system of Merapi
907 volcano, Central Java, Indonesia. *Contributions to Mineralogy and Petrology*,
908 172(4), 16.
- 909 Pichavant, M., Martel, C., Bourdier, J.L., and Scaillet, B. (2002) Physical conditions,
910 structure, and dynamics of a zoned magma chamber: Mount Pelée (Martinique,
911 Lesser Antilles Arc). *Journal of Geophysical Research: Solid Earth*, 107(B5).
- 912 Pilet, S., Baker, M.B., and Stolper, E.M. (2008) Metasomatized lithosphere and the origin
913 of alkaline lavas. *Science*, 320(5878), 916-919.
- 914 Pilet, S., Ulmer, P., and Villiger, S. (2010) Liquid line of descent of a basanitic liquid at
915 1.5 Gpa: constraints on the formation of metasomatic veins. *Contributions to*
916 *Mineralogy and Petrology*, 159(5), 621-643.
- 917 Prouteau, G., and Scaillet, B. (2003) Experimental constraints on the origin of the 1991
918 Pinatubo dacite. *Journal of Petrology*, 44(12), 2203-2241.
- 919 Putirka, K. (2016) Amphibole thermometers and barometers for igneous systems and
920 some implications for eruption mechanisms of felsic magmas at arc volcanoes.
921 *American Mineralogist*, 101(4), 841-858.
- 922 Reubi, O., and Nicholls, I.A. (2004) Magmatic evolution at Batur volcanic field, Bali,
923 Indonesia: petrological evidence for polybaric fractional crystallization and
924 implications for caldera-forming eruptions. *Journal of Volcanology and*
925 *Geothermal Research*, 138(3), 345-369.
- 926 Ridolfi, F., Puerini, M., Renzulli, A., Menna, M., and Toulkeridis, T. (2008) The
927 magmatic feeding system of El Reventador volcano (Sub-Andean zone, Ecuador)
928 constrained by texture, mineralogy and thermobarometry of the 2002 erupted
929 products. *Journal of Volcanology and Geothermal Research*, 176(1), 94-106.
- 930 Samaniego, P., Martin, H., Monzier, M., Robin, C., Fornari, M., Eissen, J.-P., and Cotten,
931 J. (2005) Temporal evolution of magmatism in the Northern Volcanic Zone of the

- 932 Andes: the geology and petrology of Cayambe Volcanic Complex (Ecuador).
933 *Journal of Petrology*, 46(11), 2225-2252.
- 934 Sato, H., Holtz, F., Behrens, H., Botcharnikov, R., and Nakada, S. (2005) Experimental
935 petrology of the 1991-1995 Unzen dacite, Japan. Part II: Cl/OH partitioning
936 between hornblende and melt and its implications for the origin of oscillatory
937 zoning of hornblende phenocrysts. *Journal of Petrology*, 46(2), 339-354.
- 938 Shane, P., Nairn, I.A., and Smith, V.C. (2005) Magma mingling in the ~50 ka Rotoiti
939 eruption from Okataina Volcanic Centre: implications for geochemical diversity
940 and chronology of large volume rhyolites. *Journal of Volcanology and*
941 *Geothermal Research*, 139(3), 295-313.
- 942 Shannon, R.D. (1976) Revised Effective Ionic-Radii and Systematic Studies of
943 Interatomic Distances in Halides and Chalcogenides. *Acta Crystallographica*
944 *Section A*, 32(Sep1), 751-767.
- 945 Sisson, T.W. (1994) Hornblende-melt trace-element partitioning measured by ion
946 microprobe. *Chemical Geology*, 117(1), 331-344.
- 947 Smith, D.J. (2014) Clinopyroxene precursors to amphibole sponge in arc crust. *Nature*
948 *communications*, 5.
- 949 Sorbadere, F., Schiano, P., and Métrich, N. (2013) Constraints on the origin of nepheline-
950 normative primitive magmas in island arcs inferred from olivine-hosted melt
951 inclusion compositions. *Journal of Petrology*, 54(2), 215-233.
- 952 Spulber, S.D., and Rutherford, M.J. (1983) The origin of rhyolite and plagiogranite in
953 oceanic crust: an experimental study. *Journal of Petrology*, 24(1), 1-25.
- 954 Sun, C., Graff, M., and Liang, Y. (2017) Trace element partitioning between plagioclase
955 and silicate melt: The importance of temperature and plagioclase composition,
956 with implications for terrestrial and lunar magmatism. *Geochimica et*
957 *Cosmochimica Acta*, 206, 273-295.
- 958 Sun, C., and Liang, Y. (2012) Distribution of REE between clinopyroxene and basaltic
959 melt along a mantle adiabat: effects of major element composition, water, and
960 temperature. *Contributions to Mineralogy and Petrology*, 163(5), 807-823.
- 961 -. (2013a) Distribution of REE and HFSE between low-Ca pyroxene and lunar picritic
962 melts around multiple saturation points. *Geochimica et Cosmochimica Acta*, 119,
963 340-358.
- 964 -. (2013b) The importance of crystal chemistry on REE partitioning between mantle
965 minerals (garnet, clinopyroxene, orthopyroxene, and olivine) and basaltic melts.
966 *Chemical Geology*, 358, 23-36.

- 967 Tappe, S., Foley, S.F., Stracke, A., Romer, R.L., Kjarsgaard, B.A., Heaman, L.M., and
968 Joyce, N. (2007) Craton reactivation on the Labrador Sea margins: $^{40}\text{Ar}/^{39}\text{Ar}$ age
969 and Sr–Nd–Hf–Pb isotope constraints from alkaline and carbonatite intrusives.
970 Earth and Planetary Science Letters, 256(3), 433-454.
- 971 Tiepolo, M., Oberti, R., Zanetti, A., Vannucci, R., and Foley, S.F. (2007) Trace-element
972 partitioning between amphibole and silicate melt. Reviews in Mineralogy and
973 Geochemistry, 67(1), 417-452.
- 974 Tiepolo, M., Vannucci, R., Bottazzi, P., Oberti, R., Zanetti, A., and Foley, S. (2000)
975 Partitioning of rare earth elements, Y, Th, U, and Pb between pargasite,
976 kaersutite, and basanite to trachyte melts: Implications for percolated and veined
977 mantle. Geochemistry, Geophysics, Geosystems, 1(8).
- 978 Toya, N., Ban, M., and Shinjo, R. (2005) Petrology of Aoso volcano, northeast Japan arc:
979 temporal variation of the magma feeding system and nature of low-K amphibole
980 andesite in the Aoso-Osore volcanic zone. Contributions to Mineralogy and
981 Petrology, 148(5), 566-581.
- 982 Vannucci, R., Piccardo, G.B., Rivalenti, G., Zanetti, A., Rampone, E., Ottolini, L.,
983 Oberti, R., Mazzucchelli, M., and Bottazzi, P. (1995) Origin of LREE-depleted
984 amphiboles in the subcontinental mantle. Geochimica et Cosmochimica Acta,
985 59(9), 1763-1771.
- 986 Vaselli, O., Downes, H., Thirlwall, M., Dobosi, G., Coradossi, N., Seghedi, I., Szakacs,
987 A., and Vannucci, R. (1995) Ultramafic xenoliths in Plio-Pleistocene alkali
988 basalts from the Eastern Transylvanian Basin: depleted mantle enriched by vein
989 metasomatism. Journal of Petrology, 36(1), 23-53.
- 990 Wade, J.A., Plank, T., Stern, R.J., Tollstrup, D.L., Gill, J.B., O'Leary, J.C., Eiler, J.M.,
991 Moore, R.B., Woodhead, J.D., and Trusdell, F. (2005) The May 2003 eruption of
992 Anatahan volcano, Mariana Islands: Geochemical evolution of a silicic island-arc
993 volcano. Journal of Volcanology and Geothermal Research, 146(1), 139-170.
- 994 Witt-Eickschen, G., Seck, H.A., Mezger, K., Eggins, S.M., and Altherr, R. (2003)
995 Lithospheric mantle evolution beneath the Eifel (Germany): constraints from Sr–
996 Nd–Pb isotopes and trace element abundances in spinel peridotite and pyroxenite
997 xenoliths. Journal of Petrology, 44(6), 1077-1095.
- 998 Wood, B.J., and Blundy, J.D. (1997) A predictive model for rare earth element
999 partitioning between clinopyroxene and anhydrous silicate melt. Contributions to
1000 Mineralogy and Petrology, 129(2-3), 166-181.
- 1001 Wulff-Pedersen, E., Neumann, E.R., and Jensen, B. (1996) The upper mantle under La
1002 Palma, Canary Islands: formation of Si–K–Na-rich melt and its importance as a
1003 metasomatic agent. Contributions to Mineralogy and Petrology, 125(2-3), 113-
1004 139.

1005 Yao, L., Sun, C., and Liang, Y. (2012) A parameterized model for REE distribution
1006 between low-Ca pyroxene and basaltic melts with applications to REE
1007 partitioning in low-Ca pyroxene along a mantle adiabat and during pyroxenite-
1008 derived melt and peridotite interaction. *Contributions to Mineralogy and*
1009 *Petrology*, 164(2), 261-280.

1010 Zanetti, A., Vannucci, R., Bottazzi, P., Oberti, R., and Ottolini, L. (1996) Infiltration
1011 metasomatism at Lherz as monitored by systematic ion-microprobe investigations
1012 close to a hornblendite vein. *Chemical Geology*, 134(1), 113-133.

1013
1014

1015 **Figure captions**

1016 Figure 1. Compositions of melt and amphibole in phase equilibrium experiments (gray
1017 dots) and partitioning experiments (yellow dots). Also shown are compositions of lavas
1018 and amphiboles in intraplate and arc settings (orange crosses) and xenoliths (red plus
1019 signs). The structural formula of amphiboles in panels d and e were calculated using the
1020 method of 13 cations excluding Ca, Na, and K described by Leake et al. (1997) for
1021 amphibole classification purpose, but for the parameterization procedure, all iron in the
1022 amphibole was assumed to be ferrous iron for reasons given in section 2.2. The
1023 partitioning data are from the compiled experiments in Table 1. Phase equilibrium data
1024 from 16 studies (Alonso-Perez et al., 2009; Blatter et al., 2013; Costa et al., 2004; Foden
1025 and Green, 1992; Gardner et al., 1995; Grove et al., 1997; Grove et al., 2003; Holtz et al.,
1026 2004; Kawamoto, 1996; Moore and Carmichael, 1998; Nandedkar et al., 2014; Nekvasil
1027 et al., 2004; Pichavant et al., 2002; Pilet et al., 2010; Prouteau and Scaillet, 2003; Sato et
1028 al., 2005). Lavas and amphiboles in intraplate and arc settings from 20 studies (Bernard
1029 et al., 1996; Buckley et al., 2006; Costa and Chakraborty, 2004; Demény et al., 2004;
1030 Gourgaud et al., 1989; Grove et al., 2005; Heliker, 1995; Mayer et al., 2013; Mortazavi
1031 and Sparks, 2004; Neumann et al., 1999; Nye and Turner, 1990; Pallister et al., 1996;
1032 Pallister et al., 2008; Pichavant et al., 2002; Reubi and Nicholls, 2004; Ridolfi et al.,

1033 2008; Samaniego et al., 2005; Shane et al., 2005; Tappe et al., 2007; Toya et al., 2005)
1034 and xenoliths from 10 studies (Chazot et al., 2005; Chazot et al., 1996; Grégoire et al.,
1035 2000; Ionov and Hofmann, 1995; Moine et al., 2001; Vannucci et al., 1995; Vaselli et al.,
1036 1995; Witt-Eickschen et al., 2003; Wulff-Pedersen et al., 1996; Zanetti et al., 1996).

1037

1038 Figure 2. Onuma diagram showing the REE and Y partition coefficients between
1039 amphibole and silicate melt measured in the partitioning studies listed in Table 1 (yellow
1040 dots). The orange lines are the best-fit parabolas to the trivalent REE and Y using the
1041 lattice strain model (Blundy and Wood, 1994; Brice, 1975; Wood and Blundy, 1997) for
1042 experiments in which there are more than 3 partitioning data.

1043

1044 Figure 3. Comparison between the experimentally measured partition coefficients to
1045 those predicted using (a) the melt composition model (Eqs. (1), (11)–(13)) and (b) the
1046 mineral composition model (Eqs. (1), (14)–(16)). Observed values are from partitioning
1047 studies listed in Table 1. The solid line represents 1:1 ratio, and dashed lines represent 2:1
1048 and 1:2 ratios, respectively. C_p^2 is the Pearson's Chi-square calculated according to Eq.
1049 (10).

1050

1051 Figure 4. Plots of amphibole-melt Sm partition coefficient against mole fractions of (a)
1052 Si, (b) Ti, and (c) Ca in the melt and (d) T, (e) Ti, and (f) Mg content in the amphibole.
1053 The partition coefficients of Sm in (e) and (f) are normalized using Eq. (17). The
1054 partitioning data are from the compiled experiments in Table 1.

1055

1056 Figure 5. Comparison between observed temperatures in phase equilibrium experiments
1057 to those predicted using the thermometer for amphibole-melt equilibria (Eq. 19). Open
1058 symbols are experiments containing melts with composition beyond the calibration range
1059 of our melt and mineral composition models (SiO_2 higher than 68.7 wt%). Sources of
1060 data: (1) Alonso-Perez et al. (2009), (2) Blatter et al. (2013), (3) Costa et al. (2004), (4)
1061 Foden and Green (1992), (5) Gardner et al. (1995), (6) Grove et al. (1997), (7) Grove et
1062 al. (2003), (8) Holtz et al. (2004), (9) Kawamoto (1996), (10) Moore and Carmichael
1063 (1998), (11) Nandedkar et al. (2014), (12) Pilet et al. (2010), (13) Pichavant et al. (2002),
1064 (14) Nekvasil et al. (2004), (15) Sato et al. (2005), and (16) Prouteau and Scaillet (2003).
1065

1066 Figure 6. Amphibole-melt REE partition coefficients calculated using the mineral
1067 composition model (Eqs. (1), (14)–(16)) and compositions of for amphiboles found in
1068 mantle xenoliths. All except the red curve labeled 1100°C were calculated assuming a
1069 temperature of 1000°C. The general effects of T and amphibole and melt composition on
1070 the amphibole-melt REE partition coefficients are also shown. Data source is the same as
1071 those in Fig. 1.

1072
1073 Figure 7. (a) Predicted amphibole-melt (blue lines) and clinopyroxene-melt (red and
1074 green lines) REE partition coefficients for mineral and melt compositions reported in the
1075 studies of Nandedkar et al. (2014) (0.7 GPa experiments, blue and red lines) and
1076 Nandedkar (2014) (0.4 GPa experiments, green lines), calculated using the melt
1077 composition model for amphibole-melt and the model of Sun and Liang (2012) for the
1078 clinopyroxene-melt. The dotted red line is the clinopyroxene-melt REE partition

1079 coefficient for a high Al clinopyroxene found in the 0.7 GPa experiment at 1040°C.
1080 Numbers on the right of each line are the experimental temperatures in °C. (b) Dy/Dy*
1081 vs. Dy/Yb ratios (Davidson et al., 2013) and (c)-(d) REE concentrations in the 0.7 GPa
1082 and 0.4 GPa melts normalized to those in the initial melt calculated using the predicted
1083 mineral-melt partition coefficients (melt composition model, Eqs. (1), (11)–(13) for
1084 amphibole) and consideration of mass balance. Subsets of the experiments are shown for
1085 clarity. In (b), red circles are 0.7 GPa melts saturated in clinopyroxene, blue circles are
1086 those saturated in amphibole, and the green circles are the 0.4 GPa melts with the
1087 experimental temperatures in °C. For (c) and (d) the numbers on the right of each line are
1088 the experimental temperatures in °C, and the cumulative percentage of the melt that has
1089 not been crystallized.

1090

1091 Figure 8. Primitive mantle normalized REE concentrations and Dy/Dy* vs. Dy/Yb ratios
1092 in samples from (a, c) Mt. Pelée in the Lesser Antilles Arc (Davidson and Wilson, 2011)
1093 and (b, d) Anatahan Island in the Mariana Arc (Wade et al., 2005). Also plotted are those
1094 in the (a, c) 0.7 GPa melts (Nandedkar et al., 2014) and the (b, d) 0.4 GPa melts
1095 (Nandedkar, 2014) calculated using the predicted mineral-melt partition coefficients
1096 (melt composition model, Eqs. (1), (11)–(13) for amphibole), consideration of mass
1097 balance, and assuming the REE concentration in the initial melts of those in the samples
1098 with lowest SiO₂ contents. Subsets of experiments with similar major element
1099 concentrations to those in the samples (Fig. S5) were used for the calculation. For (a) and
1100 (b) the numbers associated with each circles correspond to experimental temperatures in
1101 °C, and the SiO₂ content in the experimental melts. For (c), red circles are 0.7 GPa melts

1102 saturated in clinopyroxene, blue circles are those saturated in amphibole, and in (d) the
1103 green circles are the 0.4 GPa melts with the experimental temperatures in °C. Primitive
1104 mantle values are from McDonough and Sun (1995).

1105

1106 **Table Headings**

1107 Table 1. Data sources and experimental run conditions.

1108

1109 Table 2. List of recommended amphibole-melt REE and Y partition coefficients for
1110 amphiboles found in xenoliths.

1111

1112 Table 3. List of recommended amphibole-melt REE and Y partition coefficients for arc
1113 magma environment.

1114

1115 **Table footnotes**

1116 Table 1. ^an represents the number of experiments. ^bm represents the number of
1117 partitioning data. ^cMelt H₂O content shown when reported in the study. It was measured
1118 using SIMS by Tiepolo et al. (2000) and LaTourrette et al. (1995), and using micro
1119 Raman spectroscopy by Nandedkar et al. (2016), and calculated using mass balance by
1120 Adam and Green (2003) and Adam and Green (2006).

1121

1122 Table 2. Note: Calculated at different temperatures using the mineral composition model
1123 of this study and compositions of for amphiboles found in mantle xenoliths (Data source

1124 in Fig. 1). The composition of amphiboles is kept constant for the calculation at different
1125 temperatures.

1126

1127 Table 3. Note: Calculated using the melt composition model and the composition of
1128 amphiboles in the 0.7 GPa experiments of Nandedkar et al. (2014). *The set of partition
1129 coefficient at 730°C should be used with caution since the temperature is below the
1130 calibration range of our model.

1131

1132

Table 1. Data sources and experimental run conditions.

Study	n ^a	m ^b	P (GPa)	T (°C)	Dur (h)	Amph Mg#	Melt Mg#	Melt SiO ₂ (wt%)	Melt H ₂ O (wt%) ^c
Ion probe analysis									
LaTourrette et al., (1995)	1	10	1.5	1092	17.5	79.3	63.2	44.6	4.27
Tiepolo et al., (2000)	24	222	1.4	950–1075	36	36.5–100	15.1–100	41.5–54.6	2.4–6.15
LA-ICP-MS analysis									
Dalphe and Baker (2000)	7	88	1.5–2.5	1000–1100	24–100	67.0–93.0	46.4–87.3	34.1–47.1	
Adam and Green (2003)	4	27	0.5–2	1000–1050	24	73.0–78.5	48.1–54.3	39.9–46.0	6.2–13.0
Adam and Green (2006)	2	20	1.0–2.0	1050	48	78.9–80.0	51.2–56.5	39.1–41.4	10.3–14.1
Nandedkar et al., (2016)	8	98	0.7	780–1010	4–168	66.3–77.1	42.2–58.8	51.1–65.9	6.2–9.9
EMP analysis									
Adam and Green (1994)	2	8	2	1000	24	78.3–78.5	60.4–72.0	41.6–43.3	
Klein et al., (1997)	18	27	1	800–900	58–85	55.5–69.0	21.6–45.1	60.5–68.7	
Hilyard et al., (2000)	34	56	0.2–0.5	900–945	70–100	59.3–75.5	1.9–40.2	55.8–67.0	
Total range	100	556	0.2–2.5	780–1100	4–168	36.5–100	1.9–100	34.1–68.7	2.4–14.1

^an represents the number of experiments.

^bm represents the number of partitioning data.

^cMelt H₂O content shown when reported in the study. It was measured using SIMS by Tiepolo et al. (2000) and LaTourrette et al. (1995), and using micro Raman spectroscopy by Nandedkar et al. (2016), and calculated using mass balance by Adam and Green (2003) and Adam and Green (2006).

1133

1134

Table 2. List of recommended amphibole-melt REE and Y partition coefficients for amphiboles found in xenoliths.

Temperature (°C)	1100			1000			900			800		
	Min	Average	Max	Min	Average	Max	Min	Average	Max	Min	Average	Max
La	0.030	0.078	0.235	0.042	0.112	0.339	0.064	0.170	0.520	0.104	0.280	0.863
Ce	0.049	0.127	0.379	0.073	0.189	0.566	0.115	0.302	0.907	0.197	0.523	1.586
Pr	0.075	0.192	0.563	0.115	0.294	0.868	0.189	0.486	1.442	0.339	0.881	2.631
Nd	0.106	0.266	0.773	0.167	0.420	1.223	0.282	0.715	2.091	0.527	1.343	3.951
Sm	0.162	0.397	1.127	0.263	0.645	1.836	0.463	1.138	3.250	0.906	2.235	6.400
Eu	0.182	0.439	1.237	0.297	0.720	2.030	0.529	1.283	3.624	1.047	2.547	7.209
Gd	0.195	0.467	1.303	0.321	0.769	2.147	0.575	1.378	3.851	1.147	2.753	7.704
Tb	0.201	0.477	1.318	0.332	0.786	2.174	0.596	1.411	3.905	1.194	2.827	7.821
Dy	0.200	0.468	1.283	0.329	0.770	2.111	0.590	1.381	3.782	1.181	2.761	7.552
Y	0.195	0.454	1.238	0.321	0.746	2.031	0.574	1.333	3.626	1.145	2.656	7.214
Ho	0.192	0.445	1.209	0.315	0.729	1.981	0.562	1.301	3.529	1.120	2.587	7.002
Er	0.179	0.413	1.114	0.293	0.673	1.813	0.520	1.193	3.206	1.029	2.352	6.304
Tm	0.165	0.377	1.011	0.268	0.610	1.632	0.472	1.073	2.860	0.925	2.095	5.566
Yb	0.150	0.341	0.909	0.242	0.548	1.456	0.423	0.955	2.528	0.821	1.844	4.862
Lu	0.136	0.308	0.816	0.218	0.491	1.296	0.378	0.847	2.228	0.726	1.617	4.235

Note: Calculated at different temperatures using the mineral composition model of this study and compositions of for amphiboles found in mantle xenoliths (Data source in Fig. 1). The compositions of amphiboles are kept constant for the calculation at different temperatures.

1135

1136

Table 3. List of recommended amphibole-melt REE and Y partition coefficients for arc magma environment.

Temperature (°C)	1010	950	920	890	860	830	780	730*
La	0.14	0.17	0.19	0.25	0.24	0.34	0.39	0.13
Ce	0.26	0.32	0.36	0.49	0.48	0.69	0.85	0.36
Pr	0.42	0.54	0.61	0.86	0.86	1.26	1.67	0.87
Nd	0.63	0.83	0.96	1.37	1.4	2.1	2.93	1.88
Sm	1.07	1.45	1.69	2.5	2.66	4.06	6.18	5.6
Eu	1.24	1.7	1.98	2.97	3.21	4.95	7.77	8.13
Gd	1.37	1.9	2.22	3.37	3.68	5.71	9.23	11.1
Tb	1.46	2.03	2.38	3.63	4.02	6.26	10.4	14.3
Dy	1.48	2.08	2.43	3.74	4.18	6.53	11.11	17.39
Y	1.47	2.06	2.4	3.72	4.18	6.54	11.27	19.09
Ho	1.45	2.04	2.38	3.68	4.15	6.5	11.28	19.84
Er	1.38	1.94	2.26	3.51	3.98	6.24	11.01	21.48
Tm	1.28	1.8	2.09	3.27	3.73	5.85	10.44	22.34
Yb	1.18	1.65	1.92	3	3.44	5.38	9.72	22.53
Lu	1.08	1.51	1.74	2.73	3.14	4.91	8.95	22.24

Note: Calculated using the melt composition model and the composition of amphiboles in the 0.7 GPa experiments of Nandedkar et al. (2014). *The set of partition coefficient at 730°C should be used with caution since the temperature is below the calibration range of our model.

1137

1138

1139

Figure 1

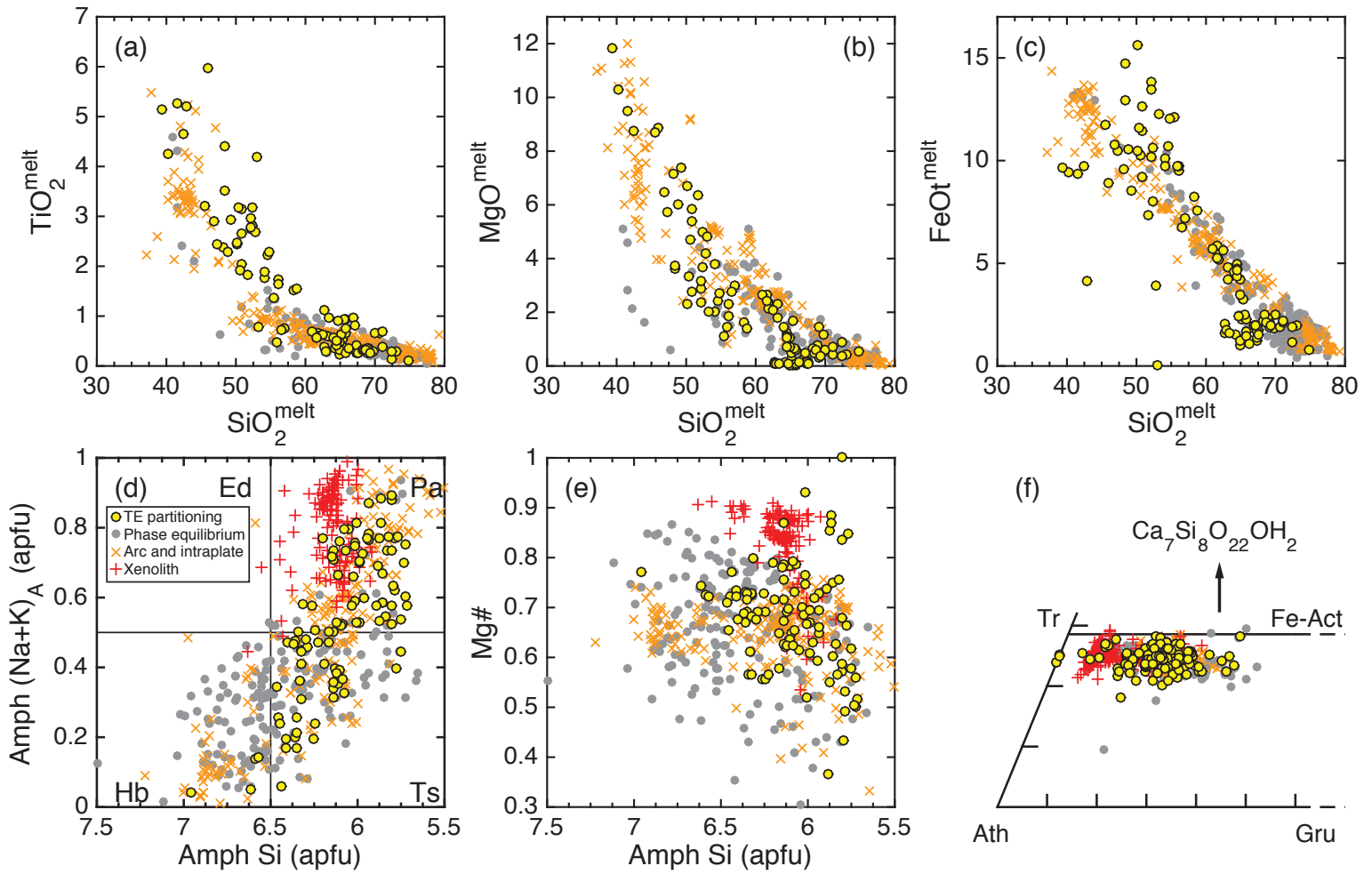


Figure 2

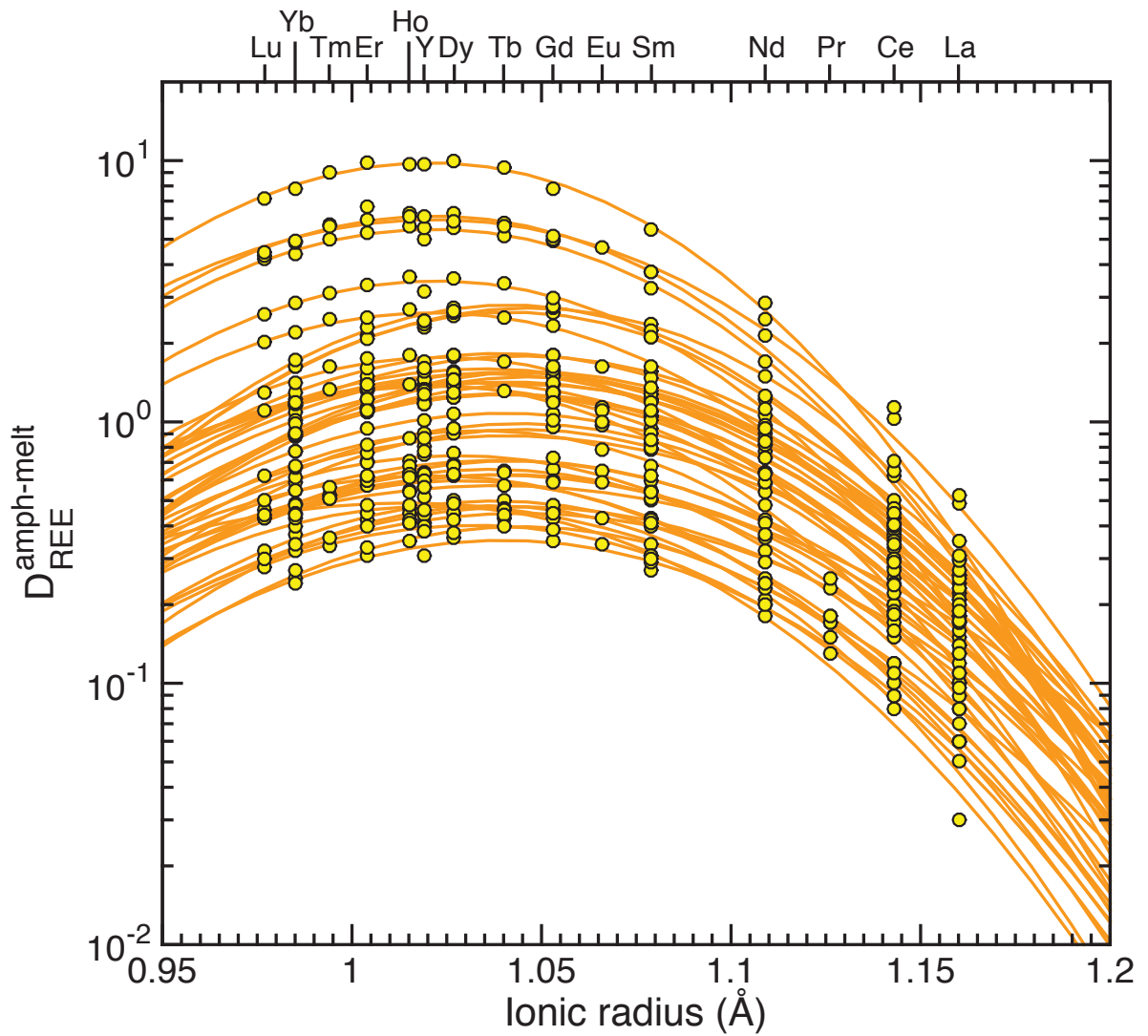


Figure 3

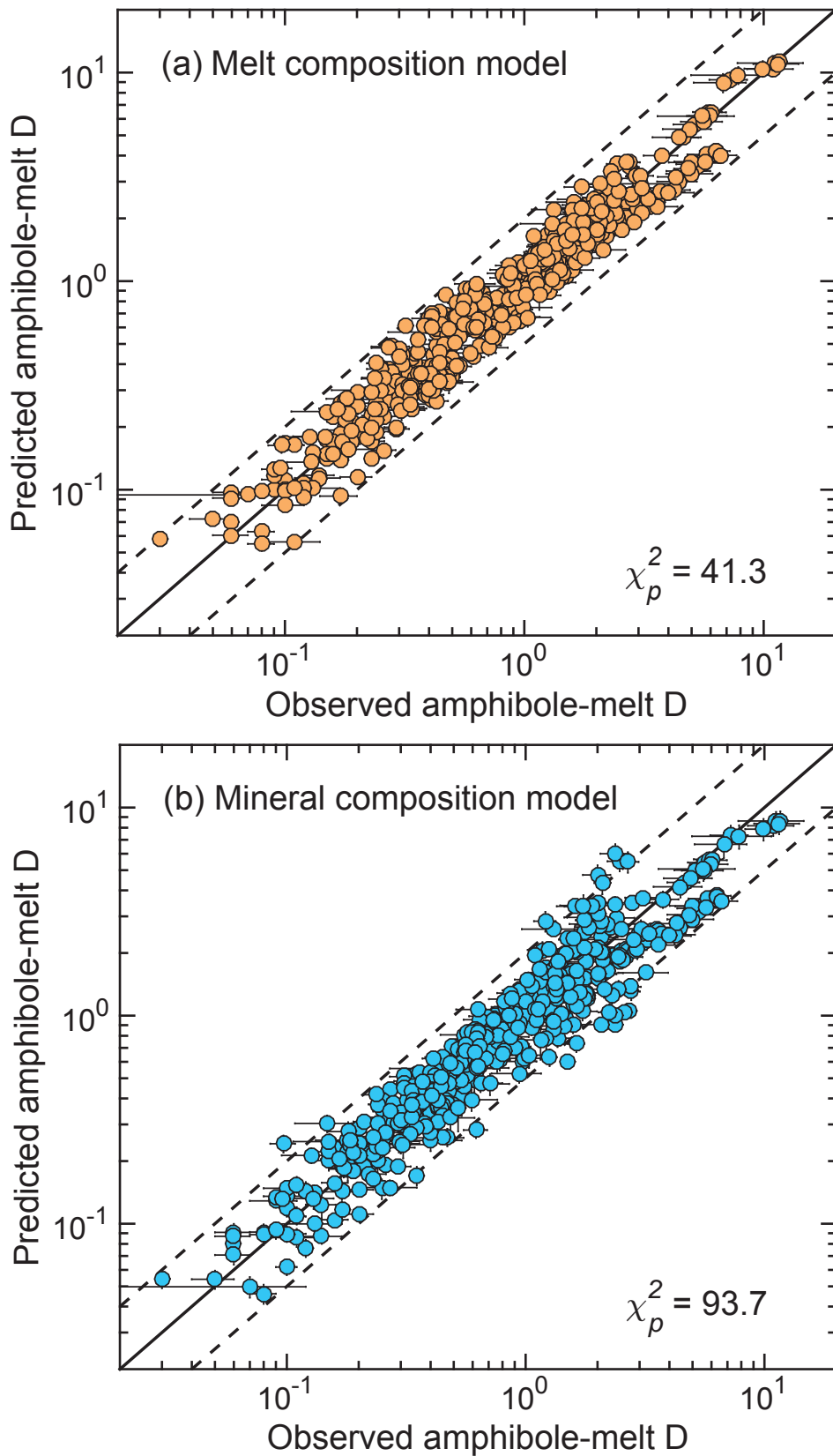


Figure 4

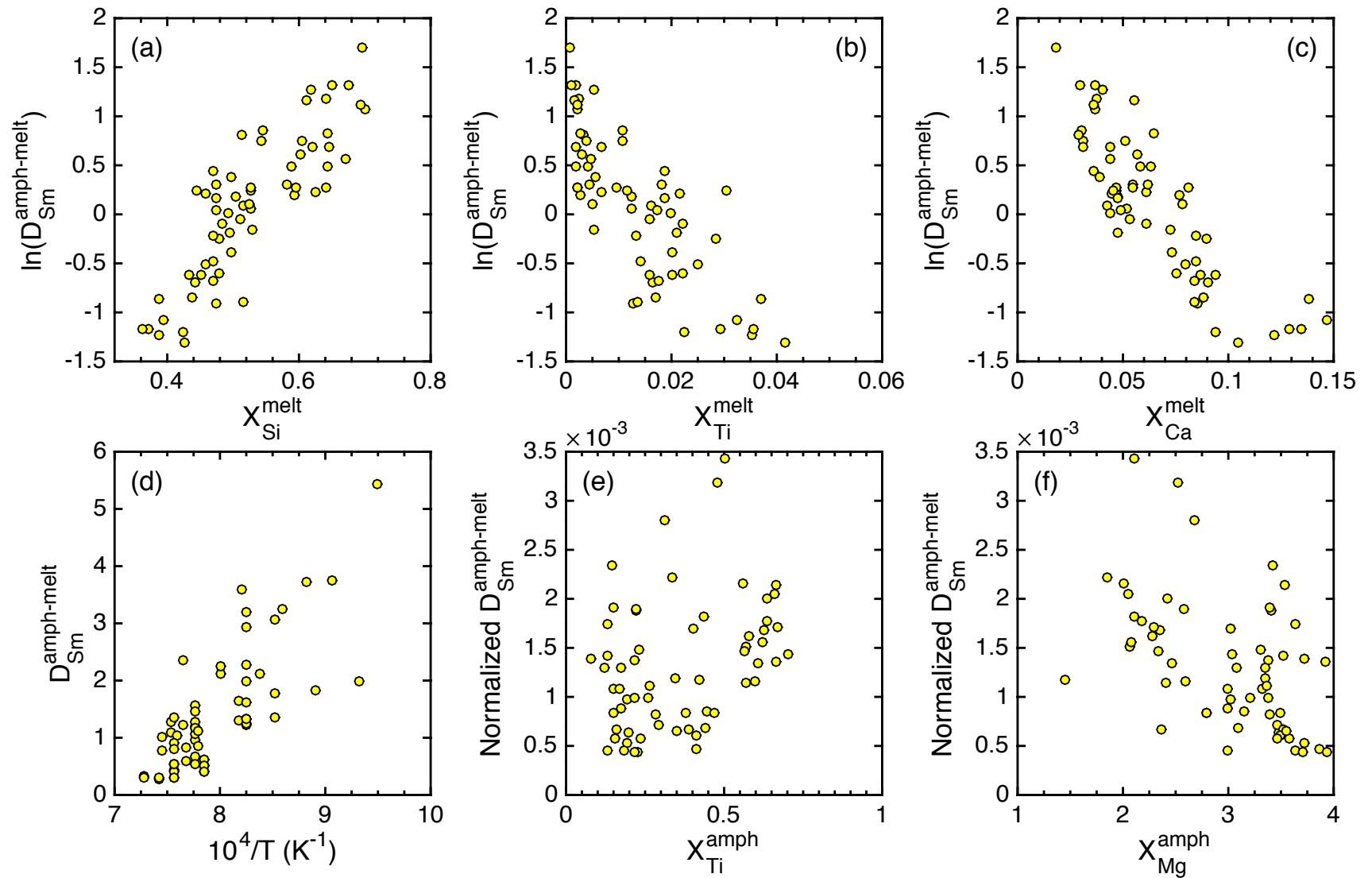


Figure 5

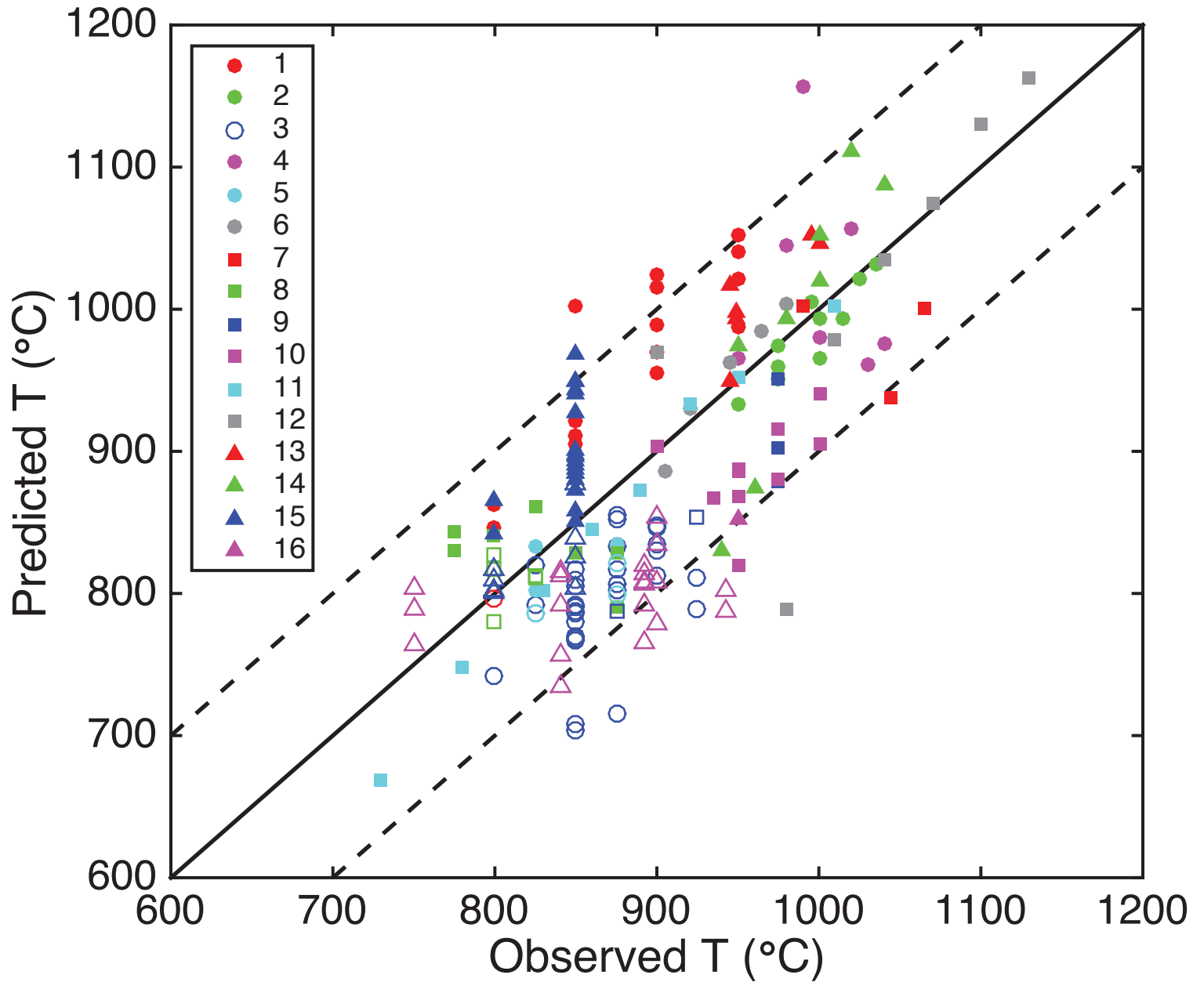


Figure 6

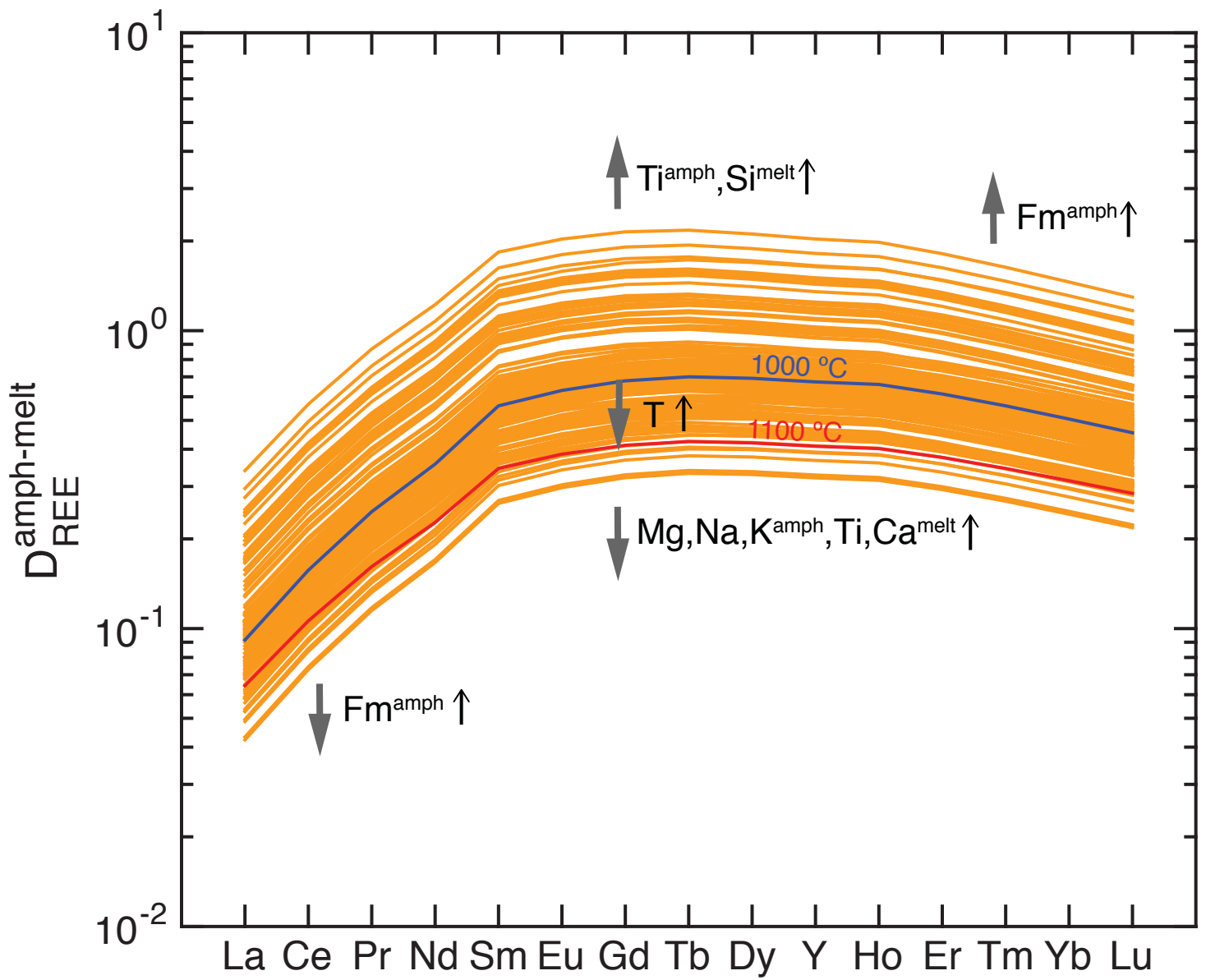


Figure 7

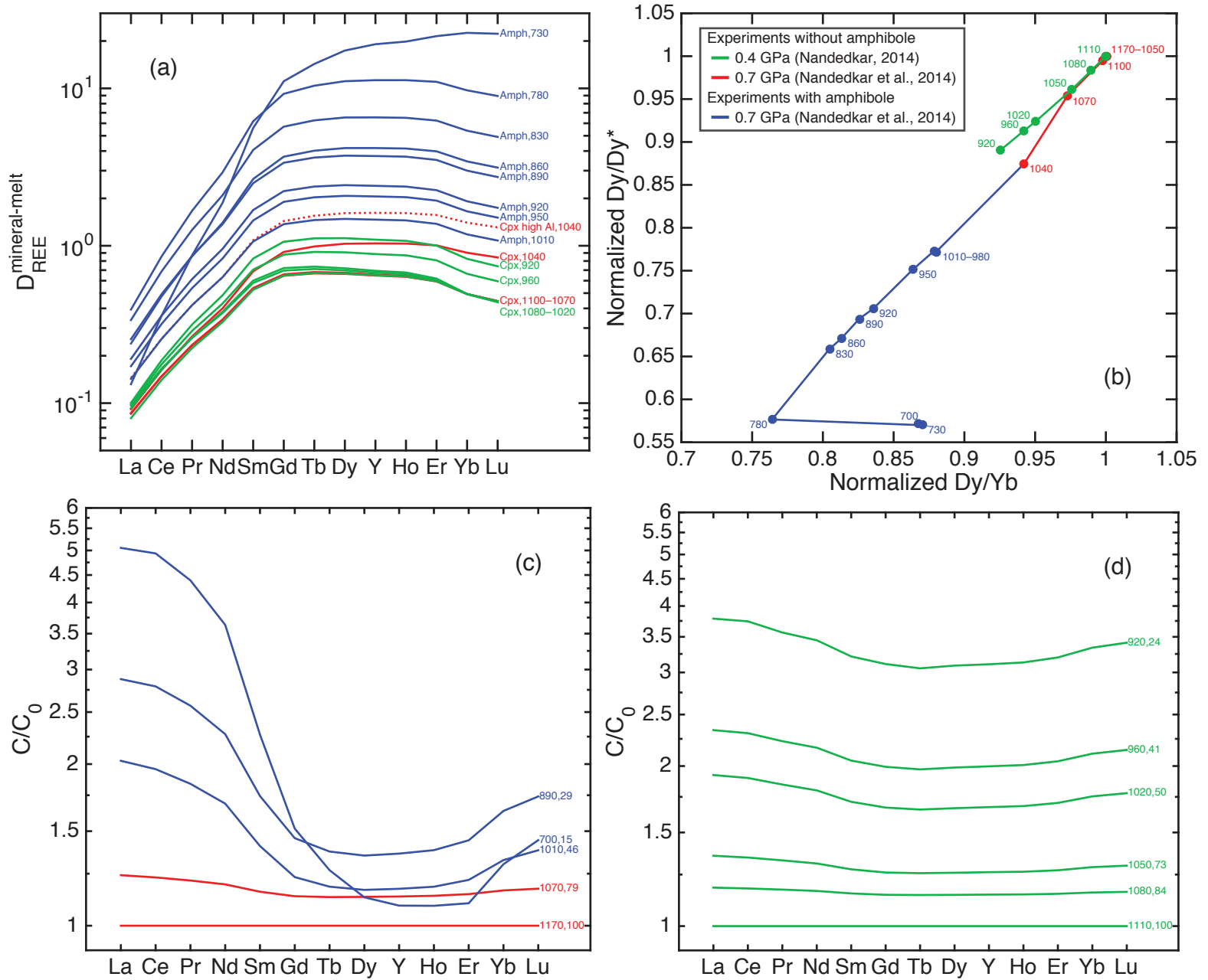


Figure 8

